8-2021

Integration of a Visible-Telecom Photon Pair Source with Silicon Photonics for Quantum Communication

Vijay Soorya Shunmuga Sundaram
vs8972@rit.edu

Integration of a Visible-Telecom Photon Pair Source with Silicon Photonics for Quantum Communication

---

M.S. *Master of Science*

in Physics

Vijay Soorya Shunmuga Sundaram

School of Physics and Astronomy

Rochester Institute of Technology

Rochester, New York

August, 2021

SCHOOL OF PHYSICS AND ASTRONOMY
COLLEGE OF SCIENCE
ROCHESTER INSTITUTE OF TECHNOLOGY
ROCHESTER, NEW YORK

M.S. THESIS DEFENSE

Candidate: .....

Thesis Title: .....

Advisor: .....

Date of defense: .....

The candidate's M.S. Thesis has been reviewed by the undersigned. The Thesis

(a) is acceptable, as presented.

(b) is acceptable, subject to minor amendments.

(c) is not acceptable in its current form.

Written details of required amendments or improvements have been provided to the candidate.

Committee:

Dr. Gregory Howland, Committee Member

Dr. Mishkatul Bhattacharya, Committee Member

Dr. George Thurston, Committee Member

Dr. Stefan Preble, Thesis Advisor

Please submit form to Physics MS Program Coordinator

SCHOOL OF PHYSICS AND ASTRONOMY
COLLEGE OF SCIENCE
ROCHESTER INSTITUTE OF TECHNOLOGY
ROCHESTER, NEW YORK

CERTIFICATE OF APPROVAL

M.S. DEGREE THESIS

The M.S. Degree Thesis of *Vijay Soorya Shunmuga Sundaram* has been examined and approved by the thesis committee as satisfactory for the thesis requirement for the M.S. degree in Physics.

_____

Dr. Gregory Howland, Committee Member

_____

Dr. Mishkatul Bhattacharya, Committee Member

_____

Dr. George Thurston, Committee Member

_____

Dr. Stefan Preble, Thesis Advisor

Date _____

INTEGRATION OF A VISIBLE-TELECOM PHOTON PAIR SOURCE WITH SILICON PHOTONICS FOR QUANTUM COMMUNICATION

By

Vijay Soorya Shunmuga Sundaram

A thesis submitted in partial fulfillment of the
requirements for the degree of M.S. in Physics, in the
College of Science, Rochester Institute of Technology.

August, 2021

Approved by

Dr. George Thurston	Date
Director, Physics M.S. Program.	

Abstract

Reliable transfer of quantum information between nodes of quantum processors and memories is crucial for the realization of many groundbreaking technologies. These include distributed sensing, distributed computation, entanglement swapping, quantum metrology, quantum key distribution etc... which would vastly expand the potential of today's quantum computers and form the framework for a secure quantum internet. However, most quantum nodes are accessed using visible photons which are incompatible with the telecom-band optical fiber network.

In this thesis, we propose a method to bridge this spectral mismatch between the quantum nodes and the communication channel using a highly non-degenerate (810nm+1550nm) photon pair source using a Periodically Poled Potassium Titanyl Phosphate (PPKTP) crystal. Previous challenges with such frequency conversion systems like spectral filtering losses, out-coupling losses and feasibility of scalable fabrication are addressed by demonstrating the successful integration of the PPKTP crystal with a Silicon Photonics Integrated Circuit (Si-PIC). Higher pair detection rates than previous studies and efficient coupling between the crystal and the PIC chip are shown. Filter-free operation of the telecom band is demonstrated by using the Silicon waveguides on the PIC for pump photon absorption for the very first time.

Contents

List of Figures

List of Tables

Chapter 1

Introduction

> *"...A quantum computer is not just a more powerful version of our current computers, just like a light bulb is not a more powerful candle. You cannot build a light bulb by building better and better candles. It is a different technology, based on deeper scientific understanding. Similarly, a quantum computer is a new kind of device, based on the science of quantum physics..."*
>
> *Dr. Shohini Ghose, A Beginner's Guide to Quantum Computing* [1]

Quantum Information Processing (QIP) is an amalgamation of information science with quantum theory and involves the encoding, communication, manipulation and measurement of information using quantum mechanical objects. It was pioneered by Richard Feynman [2] and David Deutsch [3] in the early 1980s as the only way to realistically simulate physical systems. Originally seen purely as an academic pursuit, QIP garnered increased interest in the 1990s when Peter Shor [4], Lov Grover [5] and Charles Bennett [6] published their quantum algorithms to factorize semiprimes, perform unstructured search and superdense coding, respectively. These algorithms had far-reaching implications for the field of cryptography, complexity theory and secure communication and provided an exponential timescale advantage over classical

algorithms. Since then, public and private funding towards building quantum computational systems has continued to rise leading to what's being called the NISQ - Noisy Intermediate Scale Quantum - era [7]. The NISQ era is characterized by 50-100 qubit quantum computers which are yet to be fully fault tolerant. Presently, there is active research happening worldwide into how to build quantum computers, how to program and error-correct quantum computers, and into finding new problems for quantum computers to solve.

1.1 Quantum Information Processing

The fundamental unit of QIP is the Qubit - the quantum mechanical version of a classical bit. A qubit can be any two-level quantum system with each level labelled as $|0\rangle$ and $|1\rangle$ respectively. The ability of a qubit to be in a superposition of these two states and to be in an entangled state with other qubits is what gives quantum computation the edge over classical bits. A common method of performing a quantum algorithm is by manipulating these qubits with a series of quantum logic gate operations to produce the desired outcome. Qubits have been physically realized using a number of systems as shown in fig. 1.1 below.

Qubits are extremely sensitive to external vibrations, temperature fluctuations and electromagnetic fields - any of which could cause the quantum superposition to undergo decoherence. This leads to extremely short-lived qubits making the number of qubits in a quantum computer very difficult to scale. Hence, it is equally important to be able to store qubits in *quantum memories*. Effective quantum memories would facilitate parallel processing and transfer of quantum states between quantum computers and help to overcome the really short coherence times of today's qubits. Quantum Memories have been successfully implemented using rare-earth ion-doped solids, diamond color

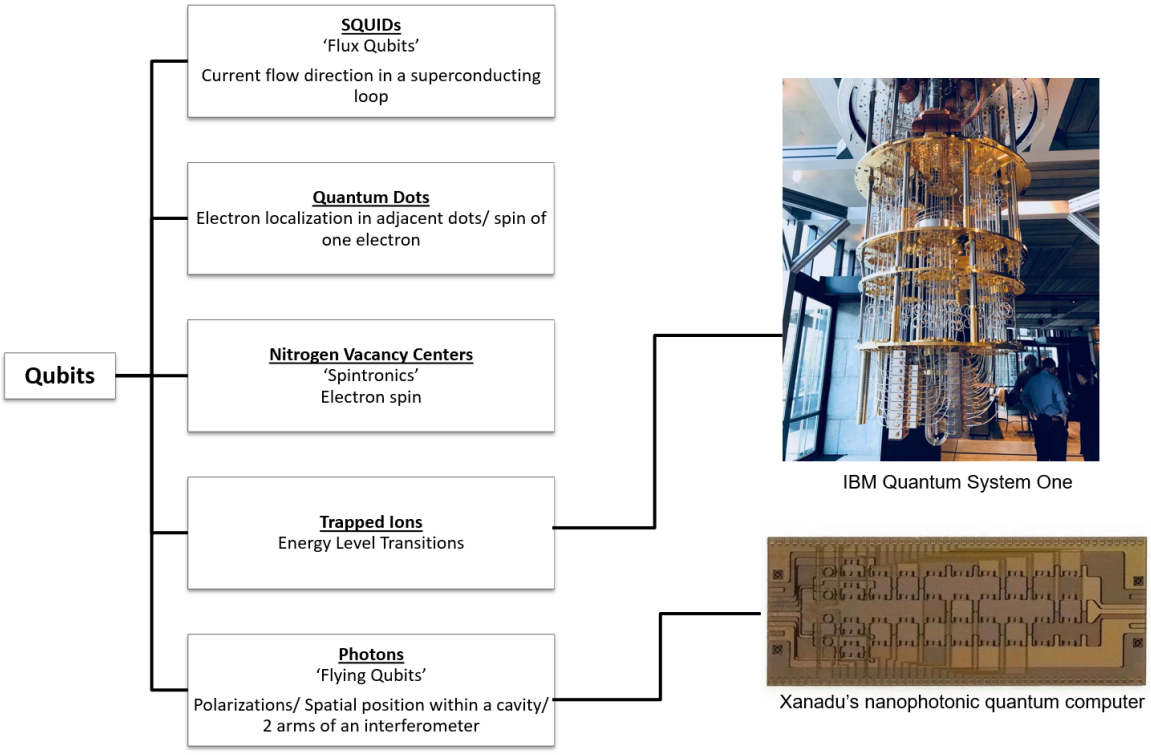

Figure 1.1: Listed are a few major physical implementations of qubits, with the different ways a two-state system is realized within each system. Two commercially available quantum computers - A trapped ion processor by IBM with 27 qubits [8] and an 8 qubit-Photonic processor by Xanadu [9] - are also shown.

centres, crystalline solids, alkali metal vapours and molecules [10]. The ability to link such processors and memories, forming a *Quantum Network* enhances the capabilities of quantum processors and also provides it's own unique applications.

1.2 Quantum Networks

A robust quantum networking scheme has many useful applications :-

1. *Distributed Computation* [11] - Presently, the state-of-art quantum computers are built of close to a hundred qubits. Scaling this number up is extremely challenging owing to the hardware requirements to control sensitive qubits and the software challenges in quantum error correction. An alternate solution would be

to emulate parallel processing similar to classical computers where parts of the problem are simultaneously solved by remote quantum computers, each handling a small number of qubits, which are linked to each other to share results over a quantum network.

2. *Quantum Key Distribution* - Sometimes referred to as the 'low hanging fruit' of quantum networks [12], quantum key distribution allows for two or more parties to securely communicate using encrypted keys generated using correlations between entangled photon pairs [13, 14]. Since existing encryption schemes can be broken using quantum algorithms, this presents a solution to the problem of secure communication in a world of quantum computers.

3. *Quantum Simulations* [15] - A collection of systems sharing quantum information, entangled with each other is fundamentally how physical matter is built. Such a many-body system can be used to perform accurate quantum mechanical simulations of molecules and chemical reactions which can be extremely useful for fundamental research and in industries such as pharmaceuticals to engineer new enzymes and vaccines faster.

4. *Quantum Metrology and Distributed Sensing* [16, 17] - Quantum Metrology deals with the use of nonclassical resources to enhance the accuracy of making scientific measurements surpassing classically determined limitations. A recent example is the Laser Interferometer Gravitational-wave Observatory (LIGO) using squeezed light to surpass the standard quantum limit due to laser shot noise to detect gravitational waves. While quantum metrology enhances the measuring capability of one sensor, distributed sensing deals with multiple sensors connected by a quantum network, leveraging their shared entangled states to probe the properties of a common object.

5. *Higher Dimensional Communication* [18] - Classically information has always been represented as a binary - 0 or 1, leading to most quantum computation schemes to be also two-level based, using qubits. However, it is possible to attain a much higher information density using higher dimensional degrees of freedom of photons. Photons in Laguerre-Gausian modes have the ability to carry Orbital Angular Momentum (OAM) which theoretically allows for an infinite amount of information to be encoded onto a single photon. Since such modes get larger with increasing OAM quantum numbers, it is the size of the optical device that limits the amount of information density. OAM based communication also offers enhanced security along with denser encoding for quantum key sharing schemes.

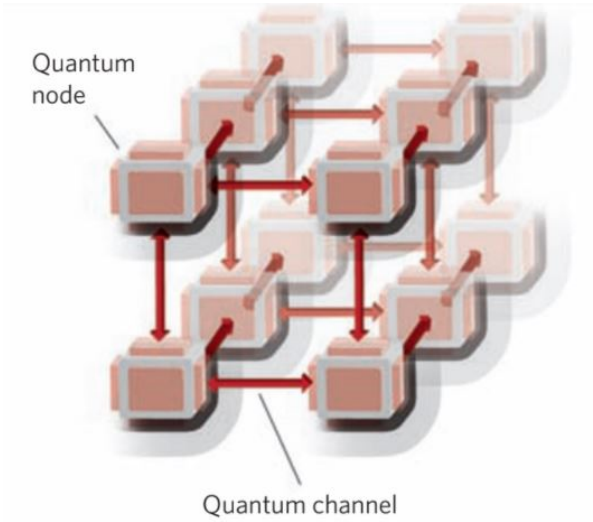

Figure 1.2: Shown is a notional quantum network composed of quantum nodes for processing and storing quantum states and quantum channels for distributing quantum information. Alternatively, such a network can be viewed as a strongly correlated many-particle system. Reproduced from [19]

A quantum network can be split into two constituent parts - the nodes and the channel, as shown in figure 1.2. The nodes can be any centers of quantum storage or processing mentioned in the previous section. The communication channel facilitates transfer of quantum states with minimal losses or decoherence. An optic channel is

typically chosen for communication owing to the speed of photons, their inert nature, ease of manipulation using linear optics and ability to interact with multiple types of nodes. Light-matter interaction schemes have been demonstrated using microcavity resonators for trapped ion systems and cold gas based quantum memories, micropillars coupled to quantum dots and Cooper pairs interacting with superconducting resonators [20, 19]. Methods to prepare a node in a desired quantum state and to read-out the quantum state without destroying the superposition or entanglement using classical laser pulses and nonclassical single-photon pulses have been extensively studied and demonstrated. A detailed review of the role of photons in QIP and the implementation of quantum algorithms using polarization encoded qubits is given in ref. [21].

One of the first trapped-ion quantum links was established between two Ytterbium ion based nodes that were 1m apart in 2006 [22] .Many other schemes for quantum communication using trapped ion nodes are elaborated in ref. [23]. The longest link between quantum nodes employing neutral atoms was demonstrated in 2012 using Rubidium atoms in a cavity in two laboratories 21m apart [24]. Nitrogen-vacancy center based nodes have also been entangled with each other over a distance of 1.3kms to demonstrate loophole-free Bell's inequality violation [25] in 2015. In 2017, quantum state transfer between two nodes of different types was performed using a cold atomic ensemble of Rb and a rare-earth-doped crystal [26]. While these experiments used different types of nodes, they all used free-space links as their communication channel. Since free-space links depend on line-of-sight communication, the maximum distance possible between nodes is limited to 143kms, beyond which the Earth tends to get in the way. Satellite-based free-space links are highly attenuated by absorption and scattering by particles and turbulence in the atmosphere. As distances increase, the wavefront of the photon expands as well and would require detectors with very large apertures to effectively detect them. Optic fibers present a much better alternative to free space

links for guiding light with minimal disturbance. Most laboratories and industries are already linked by optic fiber networks given that they are what the classical internet runs on. However, adapting existing optic fiber links to transmit quantum states in and out of nodes is presently limited due to the spectral gap that exists between them.

1.3 Node - Channel Spectral Gap

		Wavelength [nm]
Trapped ions [27]	Barium	493, 650, 1762
	Ytterbium	369, 329, 411
Neutral Atoms [28]	Rubidium	780, 795
	Cesium	852, 895
Color Centers [29]	Diamond (NV)	637
	Silicon Carbide	637-1100
Quantum Dots [30]		400-1000
Rare Earth [31]		794 [Tm^{3+}], 581 [Eu^{3+}], 619 [Pr^{3+}]

Table 1.1: Most types of quantum nodes are accessed by photons in the visible and near-IR spectrum.

As seen in table 1.1, most quantum nodes are accessed by photons at visible or near-IR wavelengths (400nm-1000nm). However, this falls within the absorption spectrum of Silicon and hence undergoes extreme attenuation over optic fiber cables. Optic fibers, on the other hand, operate at telecom-band wavelengths (1260nm-1625nm) as shown in fig. 1.3. The lowest loss is seen in the Conventional band (Telecom-C : 1530nm-1565nm). In order to use the existing optic fiber network to build a quantum network capable of linking nodes over very long distances, this spectral gap must be bridged.

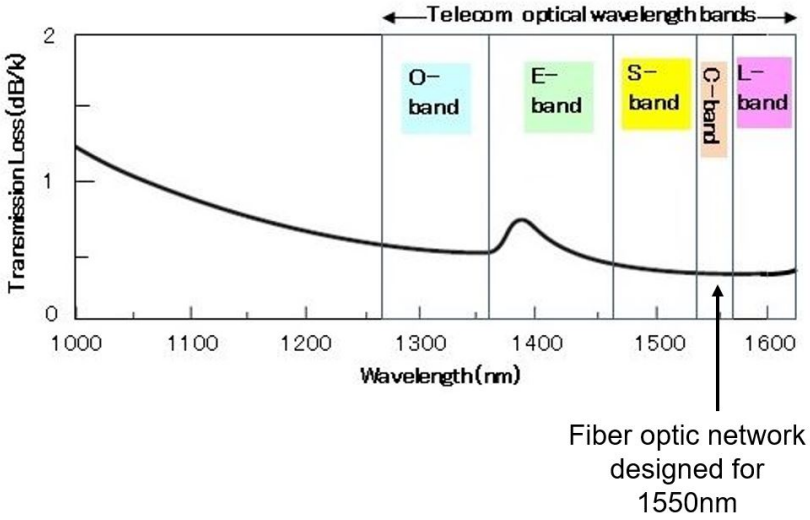

Figure 1.3: The optical fiber network exhibits the least loss in the telecom-C band close to 1550nm.

1.4 Quantum Teleportation

Classically, one way to solve the problem of lossy channels is to employ repeaters at regular intervals which receive the attenuated signal and amplify it before passing it on. While dealing with quantum information, this is not an option due to the no-cloning theorem [32] which forbids making multiple copies of arbitrary quantum states.

But, it is still possible to *teleport* a quantum state between two systems, provided the original state is no longer accessible [33]. This quantum teleportation scheme is shown in fig. 1.4.

Here, $|\psi_1\rangle$ is the initial quantum state to be teleported encoded on photon 1 with Alice, and $|\psi_2\psi_3\rangle$ is a maximally entangled Bell state encoded on a pair of photons 2 and 3. Making a joint Bell-state measurement on photons 1 and 2 yields one of four results with equal probability. Transferring this result over a classical channel to Bob allows him to make a corresponding local operation on photon 3. This maps the initial state $|\psi_1\rangle$ onto photon 3 without Alice or Bob ever having to actually measure any of the original quantum states. However, photon 1 no longer carries the initial state -

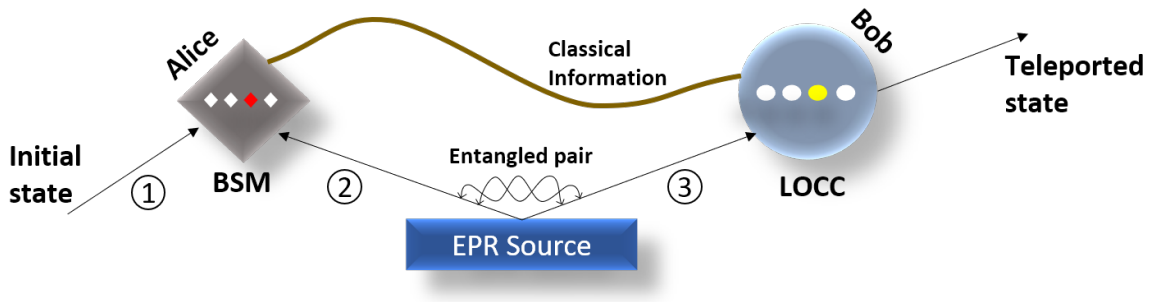

Figure 1.4: Quantum Teleportation scheme between Alice and Bob using an Einstein-Podolsky-Rosen (EPR) photon pair source - Adapted from [33]. Alice makes a joint Bell-State Measurement (BSM) and Bob performs a corresponding Local Operation after Classical Communication (LOCC) of Alice's result. This maps the quantum state of photon-1 onto photon-3.

hence no copies exist. This scheme can be used to function as a Quantum Repeater at regular intervals within a quantum network to maintain the fidelity of the signal to be transmitted. Specifically, using a highly non-degenerate photon pair source - with one photon in the visible spectrum and other in the telecom-C band - would allow existing quantum nodes to be linked via optic fiber channels as shown in fig.1.5. This work aims to identify such a highly non-degenerate photon pair source and demonstrate its scalable operation.

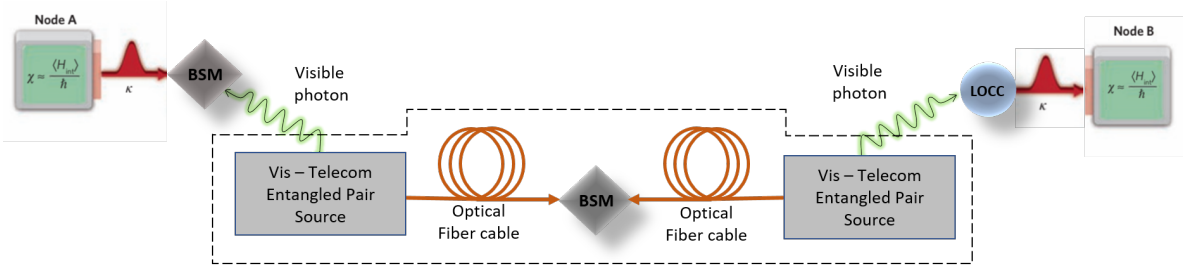

Figure 1.5: Using a visible-telecom photon pair source would allow quantum nodes to be linked via optic fiber channels across long distances. Performing a joint measurement using the visible photons from the node and the entangled pair would map the quantum state onto the telecom photon, which can then be transmitted over optic fiber channels with minimal loss.

Chapter 2

Nonclassical Photon Sources

An ideal single photon source should be able to produce photons at any arbitrary time defined by the user i.e., on demand, with 100% single photon emission probability and 0% multi-photon emission, with subsequent photons indistinguishable from each other and at an arbitrarily fast repetition rate. Historically, the single-photon regime was achieved by using extremely attenuated laser pulses. Such sources were not truly single-photon because it produced mostly a vacuum field with an occasional detection of one photon. With the emergence of quantum optics, near-ideal single photon sources have been developed across many technologies. They can be collectively classified into two classes - Deterministic Quantum Emitters and Probabilistic Heralded Pair Sources. (In practice, however, no source is truly deterministic due to losses in successfully extracting the emitted photon.) Deterministic sources are isolated quantum systems that emit only one photon upon excitation and have been realized using color centers, quantum dots, single atoms, single ions and atomic ensembles. The difficulties of these are in obtaining efficient excitation, efficient output collection, and good isolation of individual systems. They also often require specialized operating conditions such as cryogenic temperatures. A detailed review of deterministic quantum emitters can be

found in ref. [34].

Probabilistic sources are pair-emitters and generate a bi-photon field rather than a single photon. However, detection of one of the photons can guarantee the creation of the other and can be used to herald the presence of a single photon in the channel. Hence, these are also called heralded photon sources. Historically, two-photon emission in Calcium or Mercury atoms via atomic cascade was employed to produce an entangled pair of photons. However, atomic cascade methods come with similar limitations as those of on-demand emitters. These days, heralded pairs are typically generated using nonlinear processes such as Spontaneous Parametric Down Conversion (SPDC) and Four-Wave Mixing (FWM). These systems are much easier to fabricate and handle, and need no specialized operating conditions. The different types of sources, their characterization and applications can be found in ref. [35].

2.1 Nonlinear Frequency Conversion

Nonlinear optical phenomena arise when the induced polarization of a dielectic medium by an incident electromagnetic field varies nonlinearly with the strength of the field as described in equation 2.1.1 below -

$$\tilde{P}(t) = \epsilon_0 \chi \tilde{E}(t) = \epsilon_0 \left[\chi^{(1)} \tilde{E}(t) + \chi^{(2)} \tilde{E}^2(t) + \chi^{(3)} \tilde{E}^3(t) + ... \right] \tag{2.1.1}$$

- where P and E are the induced polarization and strength of applied electric field. The tilde over them denote that the quantities vary rapidly in time, following the convention in [36]. ϵ_0 is the permittivity of free space. $\chi^{(2)}$ and $\chi^{(3)}$ denote the second and third order nonlinear optical susceptibilities of the medium respectively. Typically, they are extremely small values - with $\chi^{(2)}$ on the order of 10^{-12} m/V and $\chi^{(3)} \sim 10^{-24}$ m^2/V^2. Their effects are thus barely observable unless the magnitude of E is strong enough

or the field is confined to a very small area as in the case of lasers and light guided in waveguides and optic fibers. Also, only a selective few materials exhibit sufficiently high values of $\chi^{(2)}$ and $\chi^{(3)}$ and are typically chosen for nonlinear frequency conversion.

2.2 $\chi^{(2)}$ Photon Generation

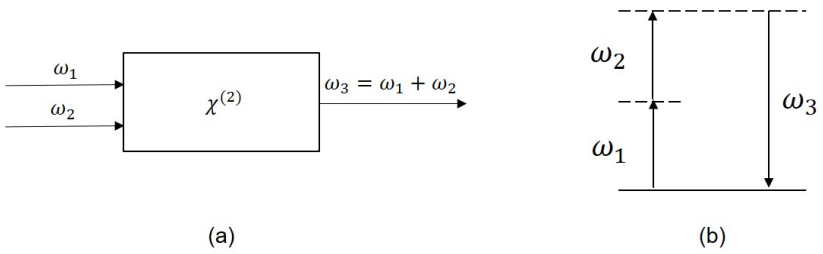

Figure 2.1: (a) Sum-Frequency Generation defines a process where the frequency of the emitted field is the sum of the frequencies of the pump field. (b) Energy level diagram describing SFG.

Certain non-centrosymmetric media (crystal lattices lacking inversion symmetry) exhibit high values of $\chi^{(2)}$ such as Beta Barium Oxide (BBO), $AgGaSe_2$, $LiNbO_3$, $KNbO_3$ and $KTiOPO_4$. When two strong electromagnetic fields, each composed of a distinct frequency ω_1 and ω_2, are incident on these materials, the polarization induced is seen to be composed of six frequency components - ω_1, ω_2, $2\omega_1$, $2\omega_2$, $\omega_1 + \omega_2$, $\omega_1 - \omega_2$ and 0. The first two correspond to direct transmission, the rest correspond to different physical processes labelled Second Harmonic Generation (SHG), Sum Frequency Generation (SFG) (shown in fig. 2.1), Difference Frequency Generation (DFG) and Optical Rectification (OR).

2.2.1 Spontaneous Parametric Down Conversion

SPDC is the time-reversed process of SFG wherein an incident pump field is annihilated to create a bi-photon field with two lower frequency components. This is classically

impossible without the presence of a weak, seed pump at either one of the lower frequencies. However, a quantum mechanical treatment of SFG shows that SPDC can occur seeded just by the electromagnetic vacuum field without the need for additional seed pumps [37, 38]. However, it is relatively inefficient and only a small fraction of the pump photons are successfully downconverted. The rest need to be removed using bandpass spectral filters.

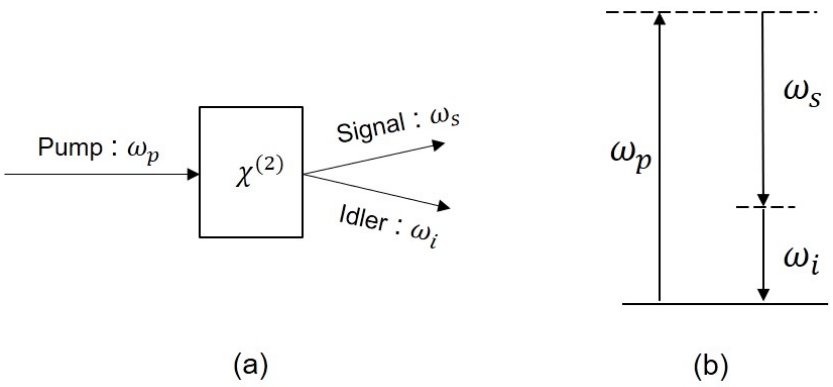

Figure 2.2: Spontaneous Parametric Down Conversion - (a) Geometric representation. (b) Energy-level Description.

Depending on the polarization of the pump photons with respect to the generated pair (usually called the signal and idler photons), SPDC can be of either Type 0, I or II. If the signal, idler and pump photons are all of the same polarization, it is said to be Type 0 SPDC. If the signal and idler photons are of the same polarization but orthogonal to the pump photon, it is said to be Type-I. If the signal and idler photons are orthogonal to each other, it is deemed type-II. Both type-I and type-II SPDC can be used to create polarization-entanglement as shown in fig. 2.3.

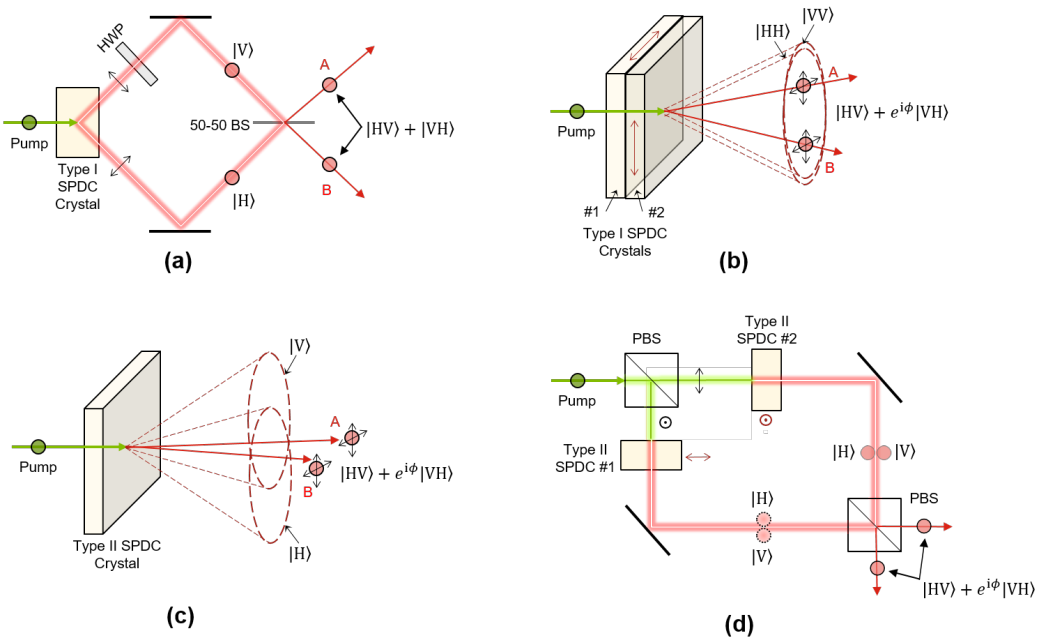

Figure 2.3: Creating polarization-entangled pairs using SPDC - (a) One of the photons from a type-I SPDC source is rotated using a Half-Wave Plate (HWP) and allowed to interfere with the other in a 50-50 Beamsplitter (BS). Postselecting photons that separated into the two output ports A and B gives the labelled entangled state. (b) Two type-I SPDC crystals are oriented orthogonal to each other and pumped with diagonally polarized photons to generate an entangled pair. (c) A type-II SPDC crystal emits orthogonally polarized photons along two conical surfaces that cross with each other at two points. Selecting photons along this crossing axis gives a pair of entangled photons. (d) Two type-II SPDC crystals, oriented orthogonal to each other, in a Mach-Zehnder interferometer can be used to generate an entangled pair by pumping the first BS with diagonally polarized photons. Adapted from [39].

2.2.2 Phase Matching Conditions

$$\omega_3 = \omega_1 + \omega_2 \quad (\textit{Conservation of Energy}) \tag{2.2.2}$$

$$\vec{k}_3 = \vec{k}_1 + \vec{k}_2 \quad (\textit{Conservation of Momentum}) \tag{2.2.3}$$

The frequency conversion processes can only occur within the limits of energy and momentum conservation given by eqns.(2.2.2, 2.2.3), collectively called the Phase Matching

Conditions.

$$\vec{k} = \frac{n\omega}{c}$$
$$\implies Eq.\ (2.2.3) \rightarrow n_3\omega_3 = n_1\omega_1 + n_2\omega_2$$
$$\therefore n_3 - n_2 = (n_1 - n_2)\frac{\omega_1}{\omega_3} \tag{2.2.4}$$

Typically, $n_1 \leq n_2 < n_3$. Therefore the left and right hand sides of Eq. 2.2.4 can't be satisfied simultaneously. However, some anisotropic materials exhibit different refractive indices based on the polarization of the incident beam - a property known as *Birefringence*. This difference can be taken advantage of to achieve phase-matching, resulting in type-I and type-II SPDC. Birefringence being an intrinsic property of the crystal is inherently limiting. There are only a few materials which exhibit high birefringence and even those allow only a limited wavelength range for tuning, especially lacking at shorter wavelengths. The phase matching is very sensitive to the temperature and orientation of the crystals, sometimes leading to awkward coupling angles. Effects like beam walk-off also diminish the efficiency of the conversion process.

2.2.3 Quasi-Phase-Matching

Insufficient or absent birefringence of a material can be compensated using a technique called as Quasi-Phase-Matching (QPM) [40]. In a non-phase-matched material, the incident and generated waves accumulate a phase shift of π over a distance known as the coherence length. This causes the amplitude of the generated field to change sign every coherence length as shown in fig. 2.4(b). By changing the sign of the nonlinear susceptibility every coherence length, the phase of the generated wave is shifted by , effectively re-phasing the interaction.

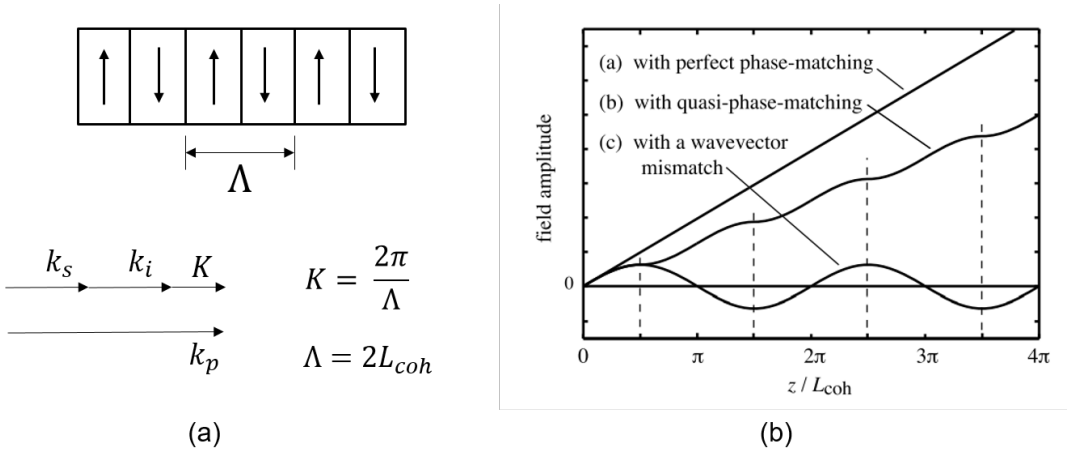

Figure 2.4: Periodic Poling to achieve Quasi Phase Matching - (a) Periodically inverted domain structure of a poled ferroelectric crystal with a period of Λ. This periodic grating compensates for the wavevector mismatch satisfying phase matching conditions. (b) Comparison of the spatial variation of the field amplitude of the generated wave in a nonlinear optical interaction for three different phase matching conditions.

This is engineered by heating a nonlinear crystal and applying a strong periodic voltage across its length to flip the sign of the nonlinearity by effectively offsetting specific ions in the crystal lattice. The period of this phase inversion can be varied to phase-match the crystal for a wide range of wavelengths.

2.2.4 Experiments using $\chi^{(2)}$ materials for visible-telecom conversion.

Owing to their high second order nonlinearity and well-established methods of poling, Periodically Poled Lithium Niobate (PPLN) and Periodically Poled Potassium Titanyl Phosphate (PPKTP) have been widely used in previous attempts to bridge the spectral gap between quantum nodes and optic fiber network. Most of the studies fall under one of two methods - Quantum Frequency Conversion (QFC) and Entangled-pair generation.

2.2.4.1 Quantum Frequency Conversion Studies

The QFC method employs DFG to directly convert the visible read-out photon from a quantum node to telecom wavelengths while preserving the quantum state. This telecom photon is then coupled into an optic fiber and measured after travelling some distance to show that the original quantum state of the node is still entangled with that of the converted photon. This has been demonstrated across different types of nodes.

In 2014, B. Albrecht et. al [41], converted a 780nm photon from a Rb-based quantum memory to the telecom-C band at 1552nm and showed successful light-matter entanglement using a second-order correlation measurement. PPLN-MgO crystal with a 1596nm pump was used for frequency conversion.

In 2018, A. Dréau et. al [42], used a PPLN crystal with a 1064nm pump to convert a 637nm photon from a Nitrogen-Vacancy center based node to 1588nm via DFG.

In 2018, T. Walker et. al [43], used PPLN to convert 894nm photons from a $^{40}Ca^{+}$ ion trap to 1530nm using DFG and showed that the quantum state is retained for up to 10km of optic fiber. While this group used a separate PPLN crystal as their seed pump, M. Bock et. al [44], showed that using an Optical Parametric Oscillator allowed them to tune the wavelength of the telecom photon across the entire telecom-O band.

Two noteworthy studies include : V. Krutyanskiy et. al [45] - transferred the quantum state of a $^{40}Ca^{+}$ ion trap over 50km of optic fiber for a total travel time of 247μs, the longest so far; and N. Maring et. al [26] - demonstrated matter-matter entanglement between a ^{87}Rb-based quantum memory and a praseodymium-doped crystal - $Pr^{3+} : Y_2SiO_5$ - using PPLN crystals. The 780nm read-out photon from the memory is converted to 1552nm using a PPLN crystal via DFG, transmitted over an optic fiber cable, and converted back to 606nm using another PPLN crystal via SFG. This 606nm photon is then used to write the quantum state into the crystal.

Since QFC employs DFG, finding a seed pump of suitable frequency and the high

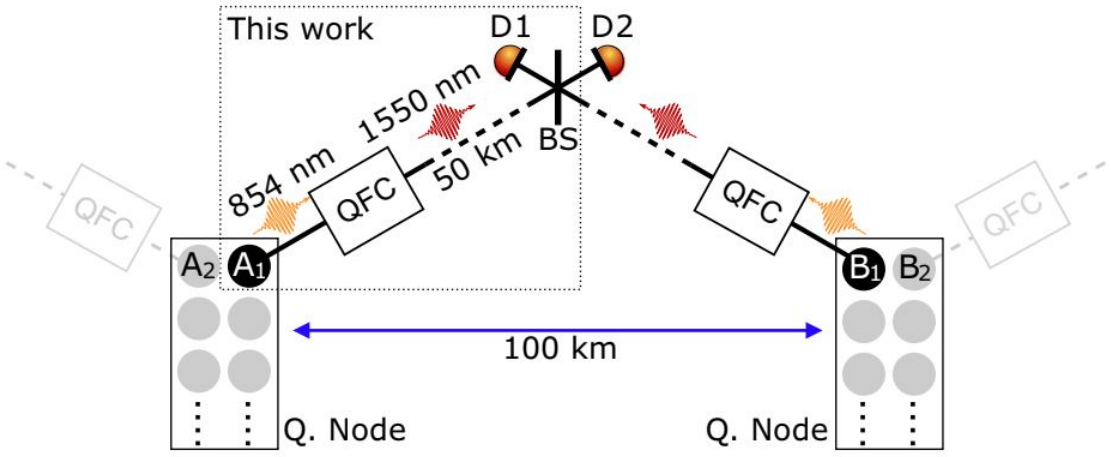

Figure 2.5: A planned QFC based quantum link between nodes that are 100m apart - reproduced from [45]. The authors propose using a multi-ion trap in place of each node to use this setup as a potential quantum repeater.

noise addition caused by this strong pump greatly limit this approach [46]. They are also limited by the maximum distance that the quantum state can be preserved for, which as of the time of writing this thesis, is 50kms. This could be used to link nodes that are up to twice that distance apart, as shown in fig. 2.5 and could be used for immediate application for small-scale networks within a city. However, for wider, potentially global networks, it makes more sense to use a highly entangled pair source for a simpler and cascadable quantum repeater circuit.

2.2.4.2 Visible-Telecom Entangled pair sources

In 2004, Potassium Niobate ($KbNO_3$) was shown to be capable of generating visible-telecom pairs at 810 and 1550nm to be used as a heralded single-photon source by S. Fasel et. al [47].

In 2014, C. Clausen et. al [48], used a PPKTP and a PPLN crystal, each producing type-I SPDC pairs at 883nm (resonant wavelength of Nd:YSO based quantum memory) and 1338nm (Telecom-O band) with a 532nm pump. The pairs are polarization-

entangled after creation using an interferometer setup similar to fig. 2.3(d). Two interleaved interferometers with appropriate telescopes and piezo-mounted mirrors were used for spatial mode matching and to compensate for the relative phase difference between the two different crystal waveguides. Spectral filtering on both arms was employed to achieve a bandwidth of 240MHz.

In 2015, O. Slattery et. al [49], reduced the bandwidth to 48MHz by placing the PPLN crystal in a doubly resonant cavity. A 894.6+1310nm pair was generated to interface between Cesium based memories and the telecom-O band.

In 2016, D. Rieländer et. al [50] also used a resonating cavity to further reduce the bandwidth to just 3MHz. The visible photon was generated at 606nm, resonant with the optical transition of praseodymium-doped crystals. The telecom photon was shown to be at 1436nm in the telecom-E band.

G. Schunk et. al [51] used a triply resonant whispering gallery mode resonator (WGMR) made of MgO doped LN wafer to generate an ultra narrow band, tunable photon-pair source. The visible photon was shown to be tunable over the $790-1064$nm for addressing the transition wavelengths of Cesium and Rubidium based memories and the corresponding telecom photons were tunable over $1064-1630$nm covering the entire telecom band.

Unlike DFG, SPDC doesn't require a seed laser and the pump can be tuned to many wavelengths, reducing the technical overhead. However, the pump still adds a high amount of background noise and the generated photons are usually extremely wide-band. This can be remedied using spectral filters or a resonant cavity but it causes the detected pair rates to be quite low compared to the generated pair rate of the crystal. Furthermore, the pairs generated also require temporal and spatial mode matching requiring more optical components. While $\chi^{(2)}$ sources are extremely bright, the size and fabrication variations involved bring down the scalability of this method.

2.3 Silicon Integrated Photonics

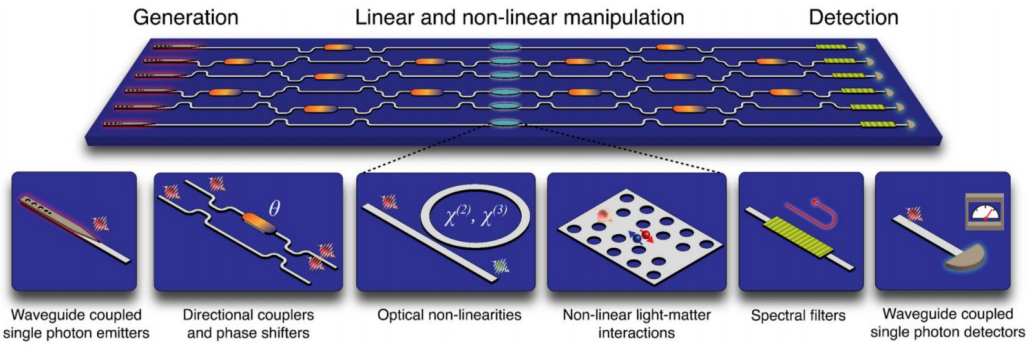

Figure 2.6: Schematic of a hybrid Silicon Quantum Photonic Integrated Circuit (Si-QPIC) consisting of modules for the generation, manipulation and detection of non-classical light. Reproduced from [52].

Silicon Photonic Integrated Circuits (PIC) provide a compact, phase-stable and high bandwidth platform to generate [53], transmit, manipulate and detect [54] light on chip as shown in fig. 2.6. The silicon-on-insulator (SOI) fabrication infrastructure is compatible with Complementary-Metal-on-Semiconductor (CMOS) technology and is highly accurate and mature, leading to a robust, high yield and reproducible opto-electronic technology [55].

While the development of quantum sources using bulk optics is quite a mature field, a more widespread adoption of quantum technologies will require the miniaturisation of devices towards the chip level. This will reduce cost, footprint, and energy consumption and greatly increase reliability compared to the bulk sources seen in the previous section. Since Silicon is a centrosymmetric crystal, it lacks second order nonlinearity. Hence, the generation of light on-chip in PICs relies on third-order nonlinear processes such as Four-Wave-Mixing. Since $\chi^{(3)} << \chi^{(2)}$, these aren't as bright as second order processes. However, it can be enhanced using very long interaction regions (spiral waveguides, long optic fiber spools) or using Optical Parametric Oscillation in resonant cavities (microring resonators).

2.3.1 Chip-Integrated $\chi^{(3)}$ Photon Sources

One of the first experiments of on-chip light generation using Si waveguides was performed by Sharping et. al [56] in 2006. Previously, FWM was only shown to produce photons in optical fibers. They were able to measure an on-chip CAR value of 25. In 2009, Clemmen et. al [57] showed photon generation in 3 PIC structures - a Si Waveguide, Sagnac loop interferometer and a ring resonator. Coincidence-to-Accidental Ratio (CAR) values of close to 40 were measured in the ring resonator, more than the other 2 structures. Further studies [58, 59, 60, 61, 62] improved upon the purity of generated single photon states and demonstrated entanglement as well. CAR values as high as 12000 and pair generation rates of approximately 1MHz have been observed [63]. However, these sources require more complex control to properly route the pump and photon pairs in/out of the resonator [64].

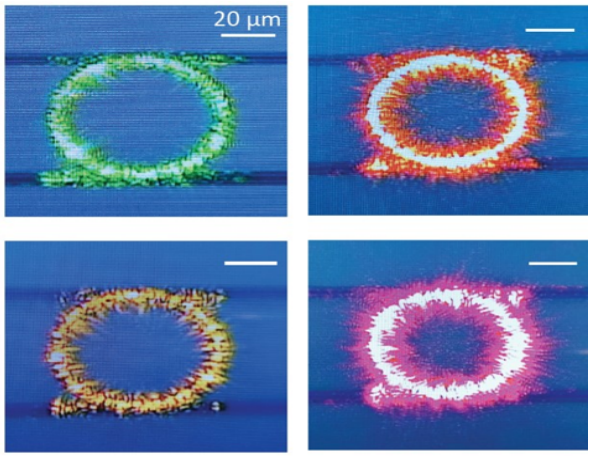

Figure 2.7: OPO output of green (568.4nm), orange (610.3nm), yellow (583.7nm) and red (665.8nm) photons in a Silicon Nitride ring resonator from [65].

Since Silicon is transparent only over wavelengths of 1.1μm, Si structures cannot be used for visible photon generation. Materials such as Silicon Nitrides (Si_3N_4) and Silicon Oxy-Nitrides (SiO_xN_y) are typically used for visible light handling on PICs but they require highly tailored dispersion and resonant control. Recently, in 2020, X Lu et

al. [65] used a silicon nitride ring resonator to generate red, orange, yellow and green photons by making very small variations in a near-infrared pump, shown in fig. 2.7.

To my knowledge, there exists only one study showing experimental on-chip generation of a visible-telecom entangled photon pair, given in ref. [66] by Lu et al. A CAR value of 3780 ± 140 and a photon detection rate up to 18400 ± 1000 pairs/sec was measured. Entanglement preservation over 20km of optic fiber was shown as well.

Chapter 3

Integrated $\chi^{(2)}$ Devices

It is worth noting that the advantages and challenges presented by bulk and on-chip photon sources are somewhat complementary to one another. Nonlinear crystal (NLC) sources, with their high values of $\chi^{(2)}$, are extremely bright but suffer from poor scalability and spectral filtering losses. Whereas, on-chip sources are extremely scalable and reliable but will not be as bright as bulk sources because $\chi^{(3)} << \chi^{(2)}$. Therefore, a natural conclusion is to integrate these two methods onto a single device. $\chi^{(2)}$ materials such as Aluminum Nitride and Thin-Film Lithium Niobate have been previously shown to successfully enable chip-scale photon sources [67]. Epitaxial Aluminum Nitride (AlN) microring resonators etched on a Sapphire substrate have been shown to be capable of producing telecom photon pairs at extremely small ring radii [68]. Thin-Film PPLN waveguides on a Silicon substrate have also been used to successfully generate cross-polarized photon pairs and time-bin entanglement [69]. However, neither of these are fully compatible with existing CMOS foundry processes and are not cost-effective.

3.1 KTP-QPIC Integration Proposal

In this thesis, we propose an alternate approach to integrating a NLC with the Silicon Quantum Photonic Integrated Circuit (Si-QPIC) platform without requiring sophisticated changes to the foundry process. Since a NLC and QPIC are most efficient at generating and manipulating photons respectively, we propose retaining those processes within their respective platforms and integrating them via simple butt-coupling as shown in fig. 3.1.

To investigate the feasibility of this method, we use periodically poled KTP waveguides as the photon source. It has been experimentally shown that poled waveguides are nearly two orders of magnitude more efficient at generating photons than bulk crystals [70]. Hence, they can give the same high outputs as a bulk crystal at much lower pump powers, greatly reducing background noise. It is also possible to integrate components like thin film $\lambda/2$ plates and directional couplers on the nonlinear waveguides allowing both type-I and II entanglement generation [71].

These generated photons can be then coupled onto a wideband Si-QPIC to provide

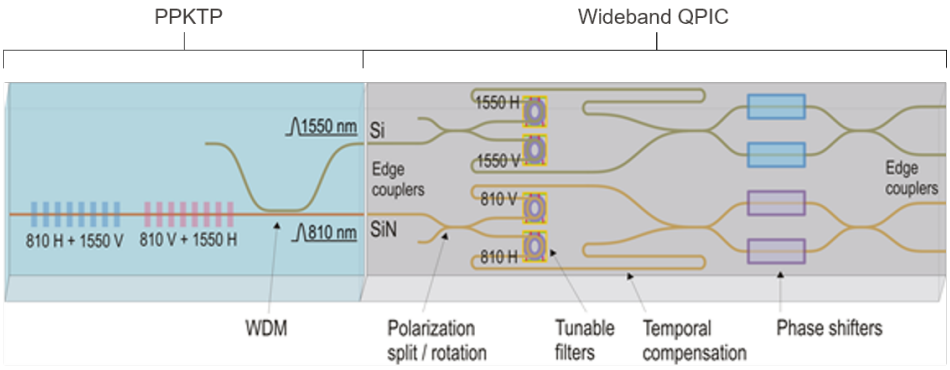

Figure 3.1: Schematic of poled KTP waveguides butt-coupled to a wideband QPIC. This combination of a highly efficient, highly non-degenerate photon pair source with a low loss, fully functional photonic circuit can be designed to provide the necessary connection between quantum nodes and communications infrastructure. A monolithic, fully packaged device allows for a robust, deployable solution towards fieldable systems in and out of the laboratory.

timing compensation and low-loss routing to on-chip circuits for quantum processing. A single QPIC can contain both Silicon and Silicon Nitride components for processing both the visible and telecom photons and can serve as a compact and reliable replacement for bulk optic circuits.

A key advantage in using Silicon waveguides is that they absorb visible photons and can be used to filter out pump noise without the losses that arise from thin-film interference spectral filters. By tailoring both the nonlinear and PIC waveguide geometries for maximum mode matching, this NLC-PIC monolithic platform would serve as a fully deployable, compact source of bright visible-telecom entangled photon pairs.

3.2 Periodically Poled KTP

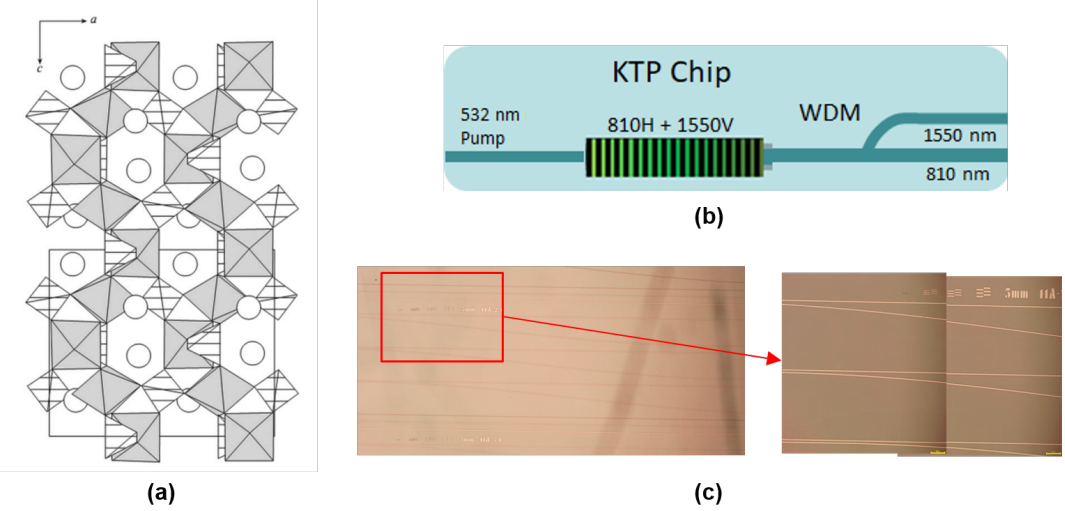

Figure 3.2: (a) Lattice structure of KTP projected onto the ac plane - Octahedra and tetrahedra are occupied by the titanium and phosphorus atoms, respectively. The circles indicate the potassium atoms, from ref. [72]. (b) The PPKTP waveguide is poled to generate a $1550 + 810$nm photon pair with a 532nm pump. Post pair generation, an on-crystal Wavelength Division Multiplexer (WDM) couples away the 1550nm photon onto an adjacent waveguide. (c) Image of the integrated WDM on KTP.

The nonlinear optical properties of Potassium Titanyl Phosphate (KTP) crystals were first discovered in 1970 and have been extensively studied since [72]. It is a non-centrosymmetric, orthorhombic crystal structure made up of a rigid three-dimensional framework of titanium-oxygen octahedra (TiO_6) and phosphorus-oxygen tetrahedra (PO_4) as shown in fig.3.2(a). Due to the mobility of K cations, KTP crystals possess high values of ionic conductivity. Polarization is caused by different positions of Ti and lengths of Ti-O bonds. KTP offers large nonlinear optical and electro-optical coefficients, a wide transparency range extending well into the UV region, high damage thresholds and low photorefraction [73]. Unlike PPLN, KTP is capable of type-II SPDC and is efficient at short wavelengths of interest (493nm and 650nm Barium emission lines, 810nm quantum dots [74]). Finally, the ability to fabricate waveguides [75] makes this platform ideal for the purpose of integration with PICs. The most promising technology to fabricate poled waveguides makes use of the rubidium-ion-exchange process. These waveguides have been shown to exhibit remarkably low propagation losses of 0.67 dB/cm [73].

The PPKTP waveguides (provided by AdvR Inc.) used in this study were poled for 0.75cm at a period of 60μm for 810(V) + 1550(H)nm pair generation using a 532nm pump laser. The chips were exchanged in a 95% $RbNO_3$ 5% KNO_3 mixture at $\sim$ 400°C for a total of 60-120 minutes, with the actual time chosen based on a resistivity measurement. Following exchange, waveguide depths at the facets were measured for the input facet and for the output facet. The chips are polished to an 8° angle at the input and 0° angle at the output. The 8 degree input is used to minimize back reflections from the 532 nm pump laser. An integrated Wavelength-Division-Multiplexer (WDM) separates the two photons onto adjacent waveguides spaced at 127μm. This WDM is essentially a directional coupler whose dimensions have been optimized for coupling at 1550nm. Separating the different wavelengths on the KTP chip allows each KTP

waveguide output coupler to be engineered for its specific wavelength to couple well to the wideband QPIC. A detailed look at the functioning of directional couplers can be found in ref.[76].

3.3 Wideband QPICs

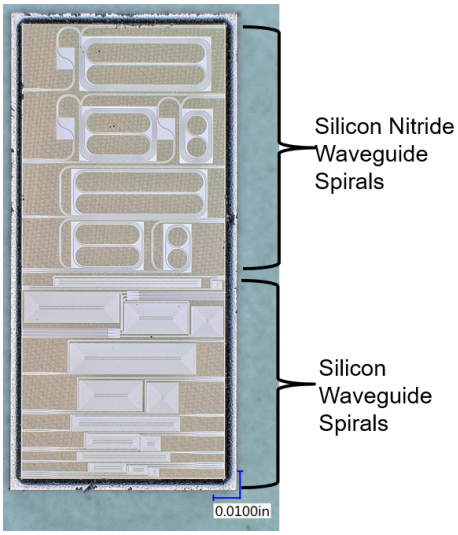

Figure 3.3: Wideband Si-QPICs containing both Silicon and Silicon Nitride components are capable of manipulating both visible and telecom photons on the same chip. The spiral waveguides allow us to demonstrate routing of photons over long path lengths with low propagation and bend losses.

A RIT-designed QPIC with both Si and SiN layers was chosen to demonstrate coupling with the KTP waveguides. This allows the handling of both the photon colors on the same chip. The chip used here has a basic array of spiral waveguides of varying path lengths as shown in fig.3.3, which can be used to demonstrate low-loss routing of photons over long distances, such as in delay lines. Future circuits can be designed with more sophisticated circuits with interferometers, directional couplers, phase shifters and so on, to achieve more complex manipulations required for quantum information processing as discussed in later sections.

Chapter 4

Methods

In order to test the feasibility of KTP-QPIC coupling, it is necessary to first quantify the losses involved in the independent systems.

4.1 Baseline Characterization of QPIC Waveguides

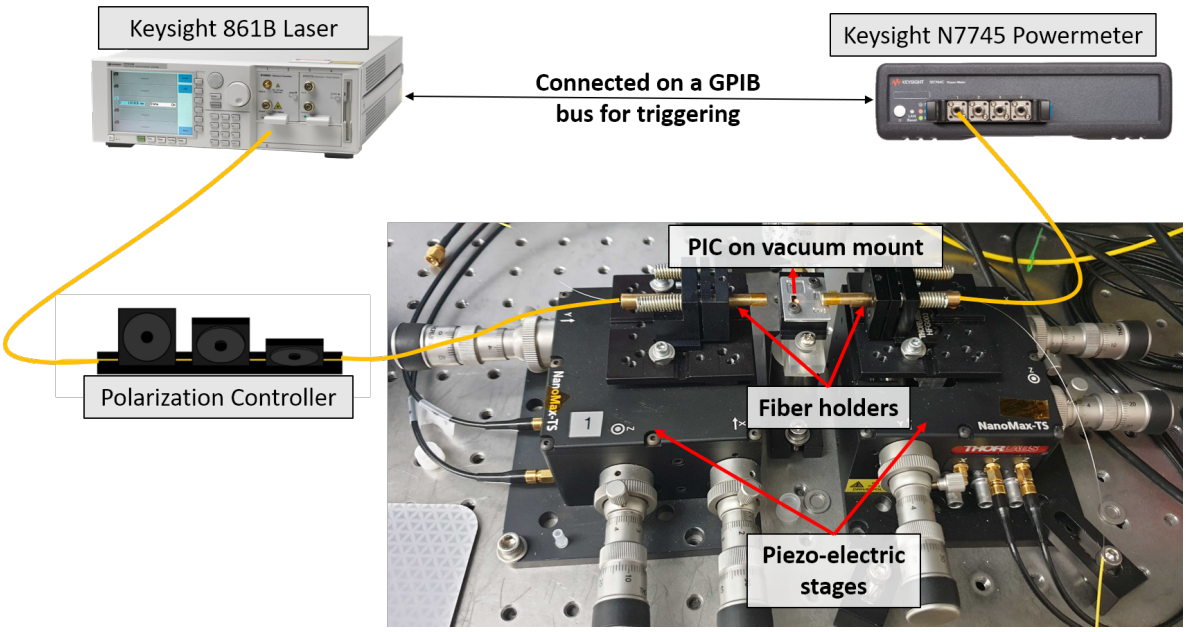

Figure 4.1: Schematic of QPIC Characterization

	1500nm	1550nm	1600nm
Insertion Loss (dB)	4.15	4.39	4.70
Propagation Loss (dB/cm)	0.59	0.74	1.08

(a) Silicon Nitride Waveguides

	1500nm	1550nm	1600nm
Insertion Loss (dB)	3.95	4.11	4.31
Propagation Loss (dB/cm)	0.30	0.26	0.20

(b) Silicon Waveguides

Table 4.1: QPIC Loss characterization results obtained from plots in fig.4.2.

A QPIC has two main sources of loss - propagation loss within the structures on the chip, which in this case are just waveguides, and insertion or coupling losses every time light is coupled in and out of the chip from a fiber. To determine both, the QPIC is held on a vacuum mount and coupled to a pair of SMF28 single mode optic fibers as shown in fig. 4.1. The fibers are mounted on a *Thorlabs 3-axis Nanomax Stage* which has a minimum travel resolution 20μm in all 3 axes, allowing for optimized coupling of the optic fibers to the edge couplers. A *Keysight 8164B* laser is used to supply 1mW of power and the output is read by a *Keysight N7744A* optical power meter. The laser is used to sweep through wavelengths of $1500 - 1600$nm and the power coupled out is recorded. This is repeated for spirals of different lengths on both the Si and SiN waveguides and the net loss is recorded as shown in fig. 4.2. The final results are tabulated in table 4.1. It can be seen that both the Si and SiN edge couplers have approximately 4.25db of coupling loss from SMF28 at 1550nm. Si waveguides also have three times smaller propagation loss than SiN waveguides.

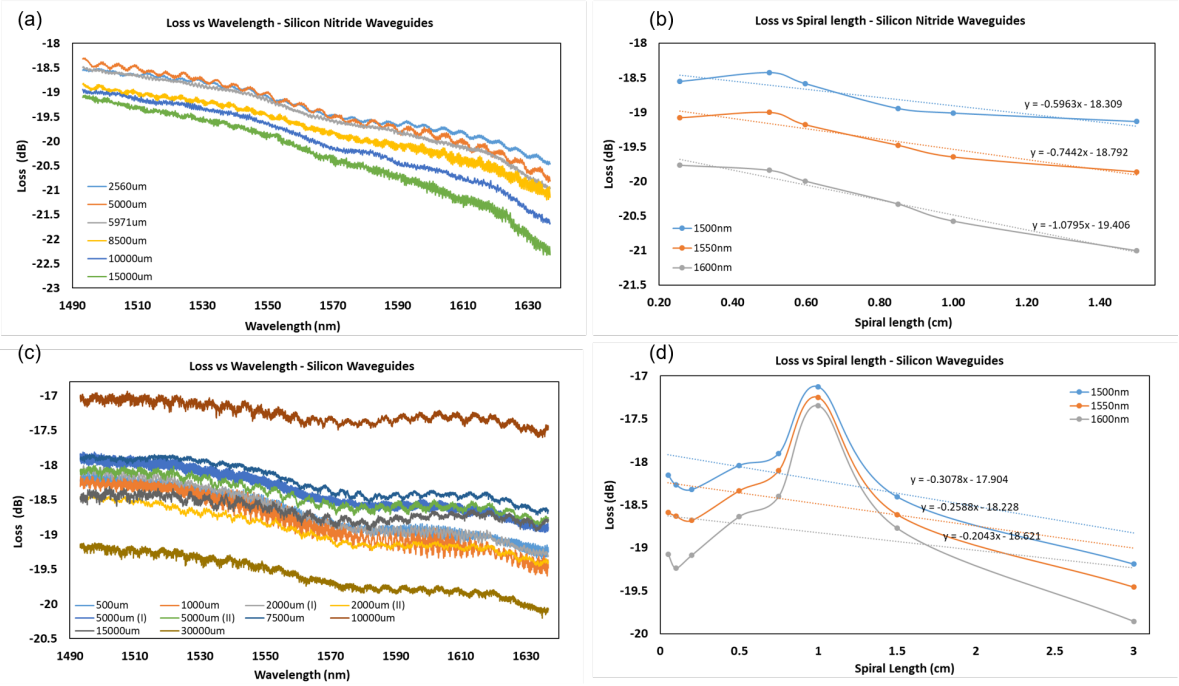

Figure 4.2: Loss is measured as the difference between the input laser power and the power coupled into the output fiber from the PIC chip (in dB). Plots (a) and (c) denote the spectral characteristics of the loss for various spiral lengths in SiN and Si respectively. Plots (b) and (d) show the variation of loss as a function of different spiral lengths at 3 fixed wavelengths -1500nm, 1550nm and 1600nm, for SiN and Si respectively. The Y-intercept of the trendline shows the loss at 0 spiral length, which denotes the insertion loss between the fibers and edge couplers on the PIC. The slope gives the propagation loss along the waveguide.

4.2 Baseline Characterization of KTP

4.2.1 Loss Characterization of KTP-SMF28 Interface

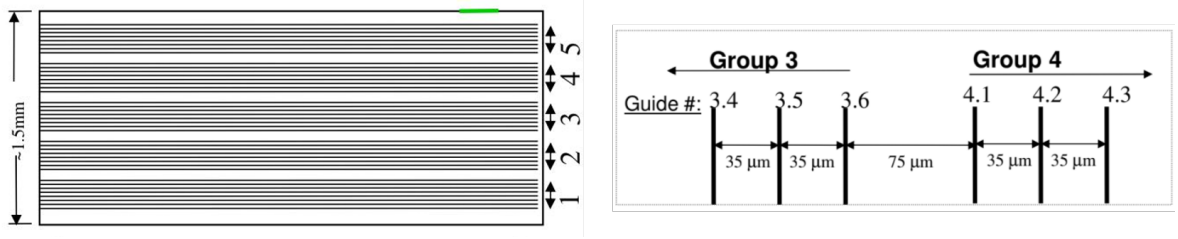

Figure 4.3: An unpoled, 'handling' KTP Chip used to measure KTP-SMF28 coupling losses. 5 groups of waveguides are etched, each with 6 waveguides of widths 2μm, 3μm and 4μm spaced 35μm from each other.

Similar to the QPIC, to characterize losses in KTP waveguides, we begin with unpoled KTP chips with groups of waveguides of different widths as shown in fig. 4.3. Since all the waveguides were of the same length, it was not possible to separately determine the propagation and insertion losses between the waveguides and the SMF28 fiber. The net loss for each waveguide was measured using the same setup as fig. 4.1 with the KTP chip taking the place of the QPIC. The best transmission was found to be close to 42% in the waveguides 1.1 and 5.2. The wider waveguides of 4μm were observed to be more lossy due to the excitation of higher modes.

4.2.2 SPDC Characterization in PPKTP waveguides

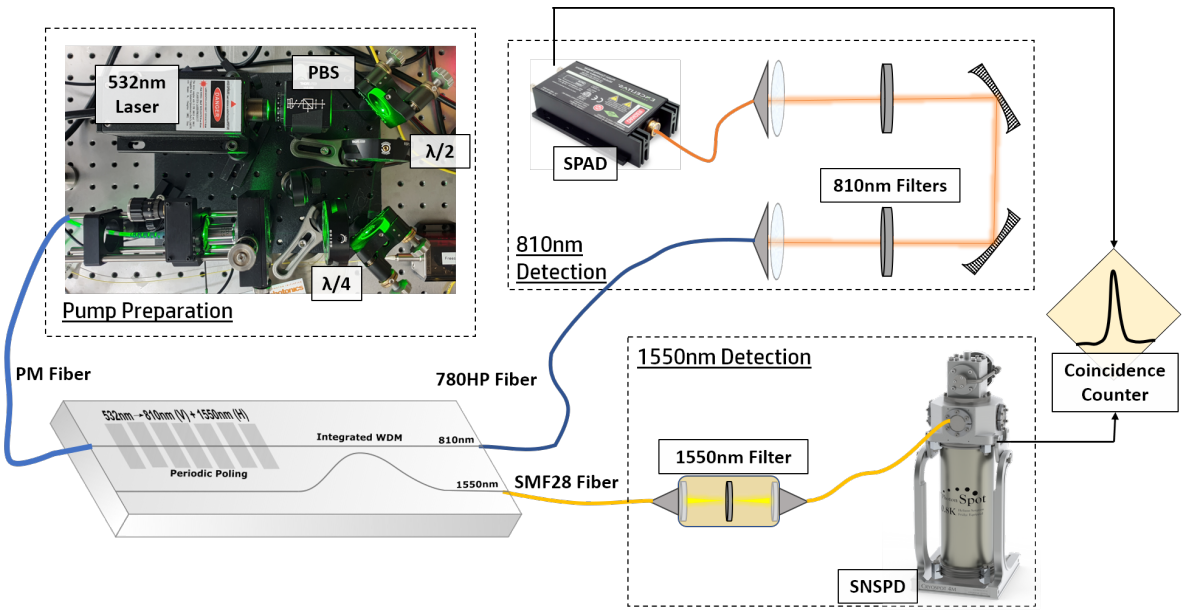

Figure 4.4: Loss Characterization of PPKTP Waveguides.

Following non-poled measurements, we were provided with poled KTP waveguides. The integrated WDM performance was already determined to be 94% efficient at routing 1550nm photons to the second waveguide. The setup to determine the SPDC pair detection rate is shown in fig. 4.4. I've separated the schematic into 3 modules to

avoid repetition in later sections where experiments are carried out with the same setup changing just one or two components. The "Pump preparation module" contains a *CNI LLL-3 DPSS* 532nm laser followed by a Polarizing Beam Splitter (PBS) to control the power output. The pump beam is prepared in the necessary polarization state using quarter-wave and half-wave plates and then coupled into a Polarization Maintaining (PM) 480 Optic Fiber. The beam is aligned precisely by moving the two mirrors for maximized coupling into the fiber.

This fiber is connected to the pigtailed fiber on the KTP, which has already been attached for ideal coupling to the input waveguide with minimal reflections. 810+1550nm pairs are generated in the waveguide and subsequently separated by the integrated WDM onto adjacent waveguides. The 810nm waveguide is then coupled to a *Nufern* 780HP fiber and carried to the "810nm detection module", which uses a narrowband *Thorlabs FBH810-10* thin film interference filters to remove any pump noise. It is coupled back into a multimode fiber for detection using a *SPCM-EDU CD3375H* Single Photon Avalanche Photodiode (SPAD).

The 1550nm waveguide from the KTP is coupled to a SMF28 fiber and routed to the "1550nm detection module". The telecom photon is filtered using a *Edmund Optics 1550/25nm 87-822* bandpass filter and subsequently detected using a *Cryospot 4* Superconducting Nanowire Single Photon Detector (SNSPD). The SPAD and SNSPD output triggers are sent to *Picoharp 300*, a Time-Correlated Single Photon Counting System (TCSPC) to measure coincidences. To account for the saturation of the detectors at high powers, a saturable-absorption model was employed to fit the data [77].The curve is given by the equation $y = \sigma x/(1 + \rho x)$ where σ represents the linear response for small pump powers and $1/\rho$ is the power necessary to achieve half of the maximum rate.

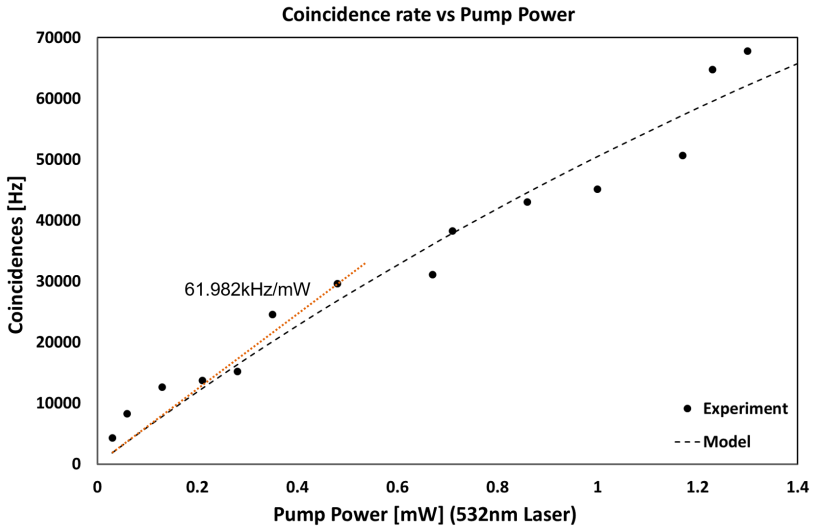

Figure 4.5: SPDC in PPKTP Waveguides - Coincidence rates as a measure of pump power : The linear slope at low powers determines the pair detection of this system to be 61.982kHz/mW.

The pair detection rate is given by σ, and was determined to be $\sim$ 62kHz/mW as shown in fig.4.5. Given that the output waveguides were spaced exactly 127μm apart while a SMF28 fiber has a cross-section diameter of 125μm, it was quite challenging to get two fibers perfectly parallel next to each other for optimized coupling.

4.2.3 Telecom Bandwidth Measurement

The generated visible band was already characterized by AdvR to be extremely narrow with a center wavelength of 812nm. For a 532nm pump, this corresponds to a wavelength of 1544nm for the telecom photon. We were able to determine the telecom band characterstics by switching out the thin-film interference filters in the 1550nm detection module to a *JDS Uniphase Tunable Fabry-Perot Etalon Filter* as shown in fig.4.6(a). By varying the voltage applied, this enables us to tune the allowed wavelengths through the filter. It was found that the generated telecom photons were centered around 1543.7nm as expected. The Full-Width at Half Maximum (FWHM) was determined

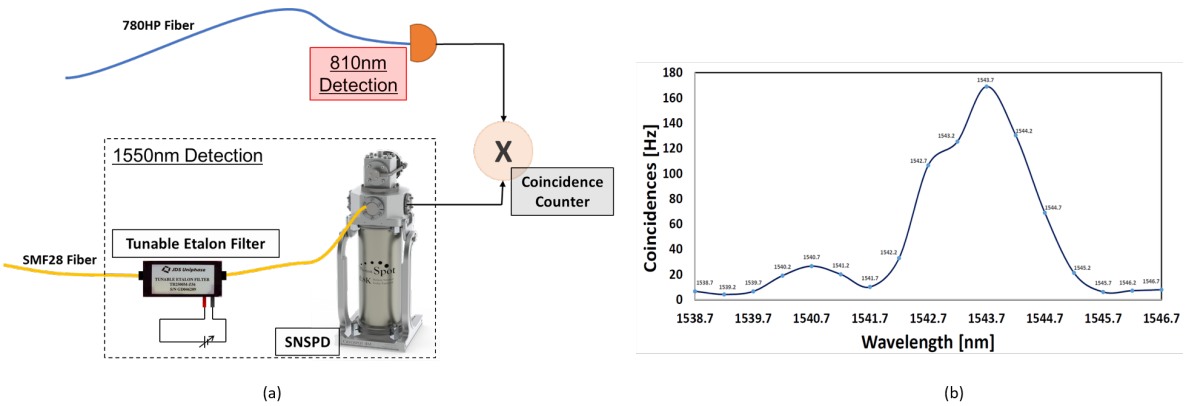

Figure 4.6: Telecom bandwidth estimation - (a) Using a tunable-filter enables fine selection of photons allowed to be detected. (b) The PPKTP waveguides generate telecom photons of ultranarrow bandwidth $\sim$ 2.2nm, with a center wavelength of 1543.7nm in the telecom O band.

to be $\sim$ 2.2nm as shown in fig.4.6(b), which is comparable to previously demonstrated ultranarrowband sources with 3nm bandwidths.

4.3 KTP-QPIC Integrated Setup

4.3.1 Coupled to Silicon Nitride Waveguide with Filtering

Next, the previously characterized QPIC is introduced next to the PPKTP chip. As shown in fig. 4.7(a), the QPIC is slightly raised from the handling wafer creating an indented shelf running around its edges, making it difficult to bring the edge couplers sufficiently close to the KTP for coupling. Hence the KTP chip was held upside down over a very thin piece of glass diced from a cover slip. This allowed us to bring the edge couplers on the QPIC right next to the KTP waveguides while giving us just enough room to bring in an optic fiber to couple to the 810nm waveguide on the KTP. A picture of this coupled setup can be seen in fig. 4.7(b). The 1550nm photon is routed through a 1.5cm long SiN spiral waveguide before being coupled out to a SMF28 fiber. The photons are once again filtered to remove pump light and coincidence measurements

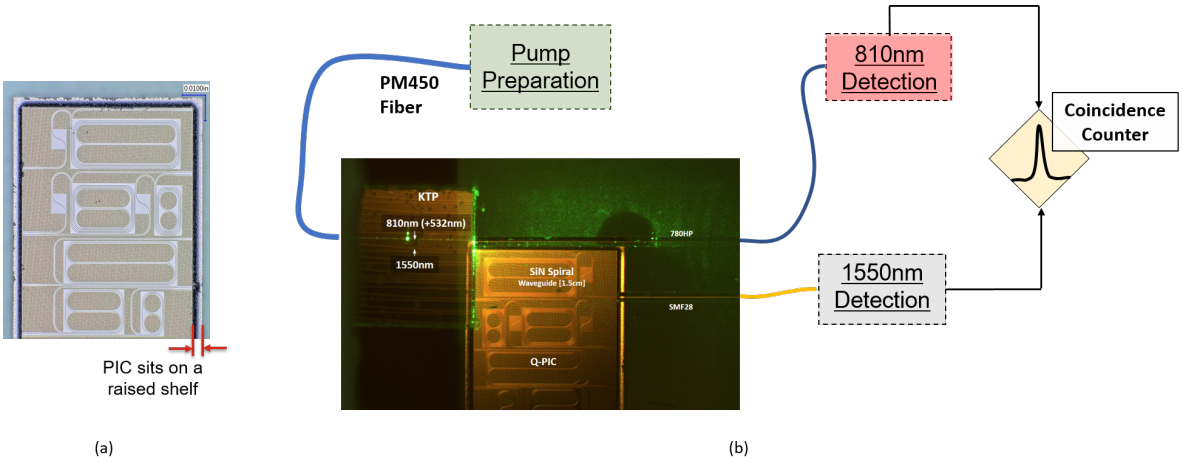

Figure 4.7: Hybrid PPKTP-QPIC Integrated Setup - (a) Image of the QPIC showing the raised edge around it. (b) The KTP is inverted so the waveguides are facing down and they can be brought right next to the edge couplers on the QPIC. The pump preparation and detection modules are the same as the KTP characterization setup.

are taken. The Picoharp also lets us monitor the single counts from each detector. The data recorded is given by the plots in fig. 4.8.

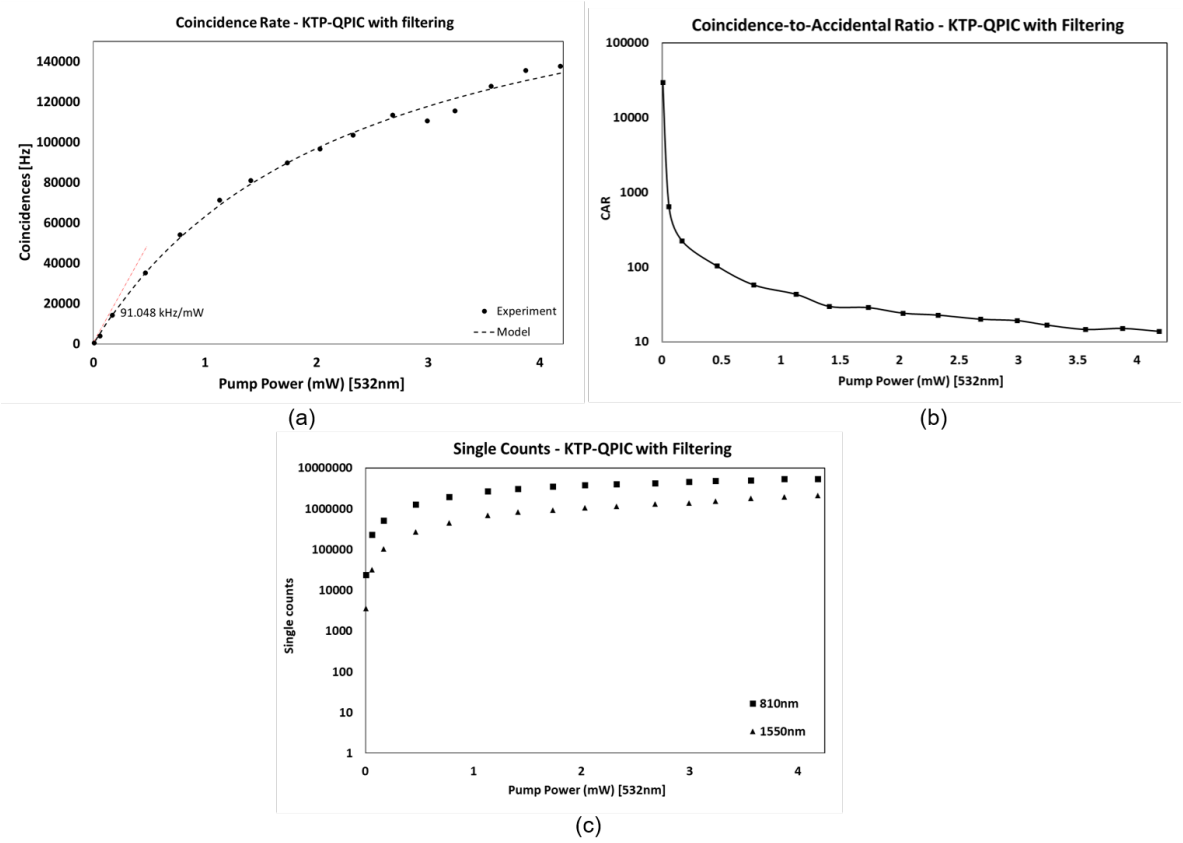

Figure 4.8: (a) The coincidence detection rate is given by the linear slope at low powers as 91.048kHz/mW. (b) A peak CAR value close to 30,000 was measured at sub-milliwatt pump powers. (c) Single counts on the orders of 10^6 were observed in the visible band while the telecom band was slightly lower. Since they are created in pairs, slightly fewer counts of 1550nm photons denote that the telecom channel is lossier than the visible channel.

4.3.2 Coupled to Silicon Waveguide without Filtering

With the KTP chip inverted, it was not possible to couple it to any of the Si waveguides on the QPIC while also allowing room for an optic fiber to reach the 810nm KTP waveguide. Therefore, a different QPIC was chosen which allowed us to dice the indented ledge on one of its edges without damaging the edge couplers. To access the visible waveguide, a portion of the chip was diced across to create a 'channel' for the fiber to get through as shown in fig. 4.9. This way, the KTP no longer needed to be

inverted and there was a wider separation between the 2 output fibers making it easier to control them for better coupling. However, it is no longer a long spiral waveguide, but just a single straight section of length 2mm. The insertion losses in this QPIC are also much smaller at just 1.5dB.

To test the Si waveguide's ability to filter out residual pump photons, the spectral filters in the 1550nm detection module were removed. However, the fiber collimators were left in place to get rid of any scattered pump light that might have coupled into the cladding of the fiber. No changes were made to the rest of the experimental setup. The results of this experiment are shown in fig. 4.10.

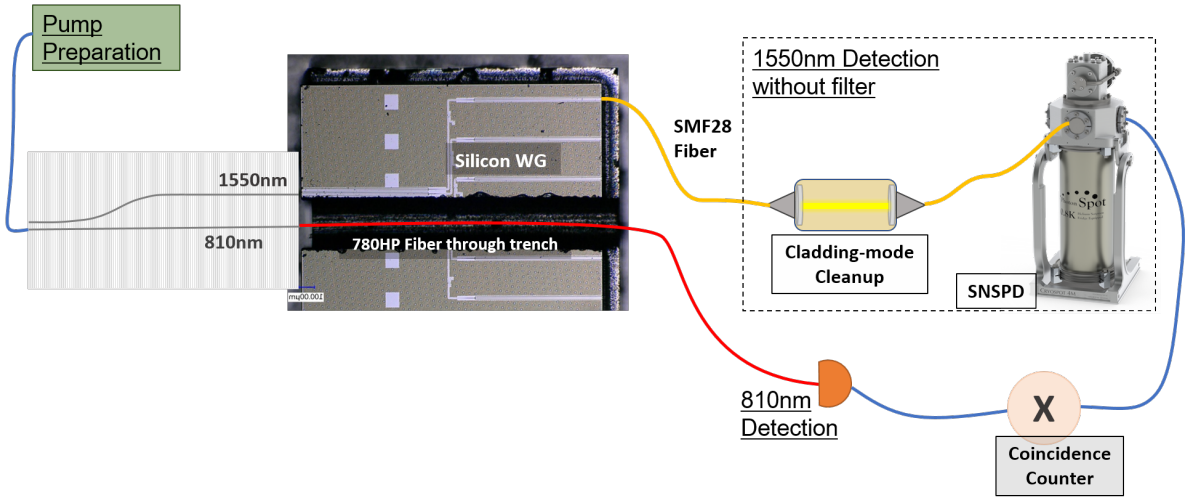

Figure 4.9: Schematic to test filterless operation of the KTP-QPIC setup - The thin film interference filters are removed from the 1550nm detection module. However, the fiber-optic collimators are left in place to ensure removal of any residual light in the cladding of the fiber.

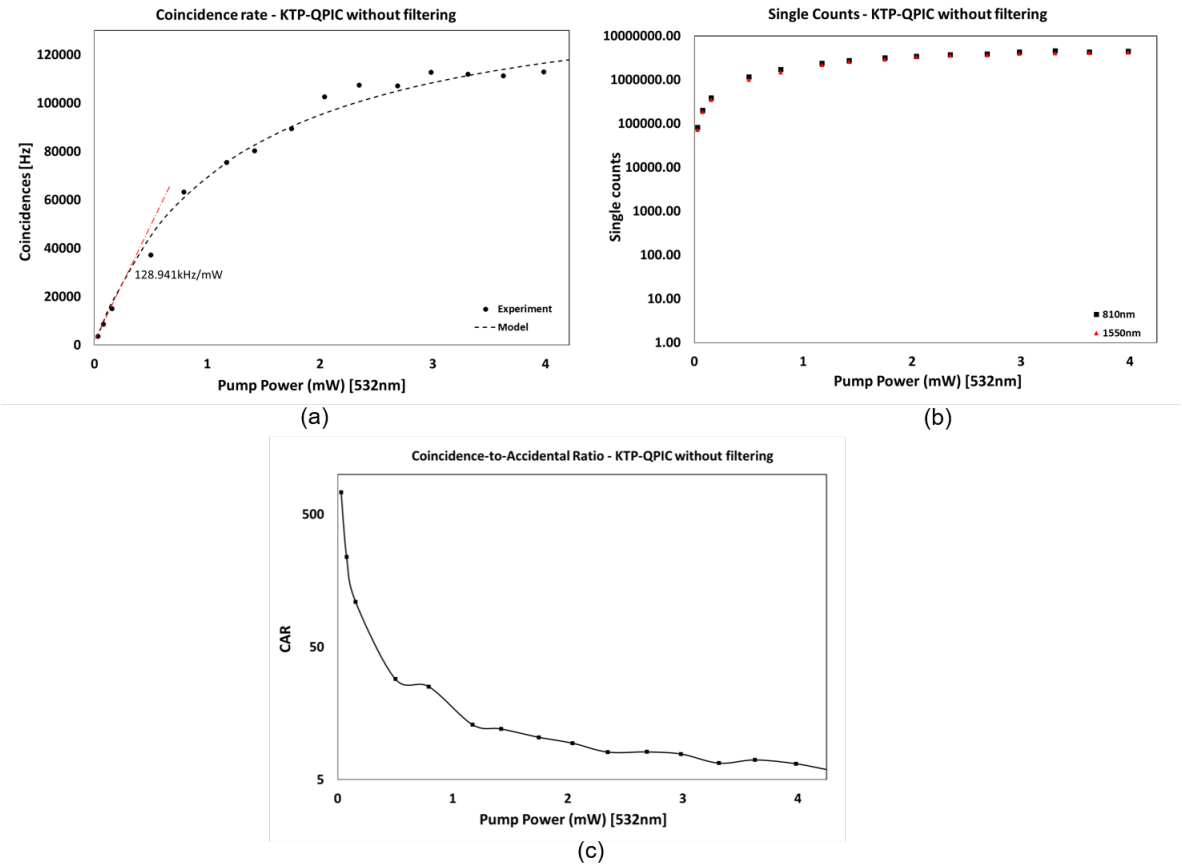

Figure 4.10: (a) The Coincidence detection rate was measured to be 128.941kHz/mW, significantly higher than the results with spectral filters in. (b) The single counts are now both on the orders of 10^6 as expected. (c) The peak CAR value has now dropped to ~ 800 compared to the filtered operation.

4.4 Second-order Correlation Measurement

The key issue with heralded single-photon sources is whether or not the heralded state is indeed a single photon. This is typically determined by measuring the degree of second-order coherence ($g^{(2)}(\tau)$) for the heralded field, conditioned on detection of the heralding signal. For realistic sources, $g^{(2)}(0) < 0.5$ is required to claim a single-photon state since the theoretical value for a two-photon Fock state is 0.5 [78]. The closer the value is to zero, the better the source approaches a true single-photon source.

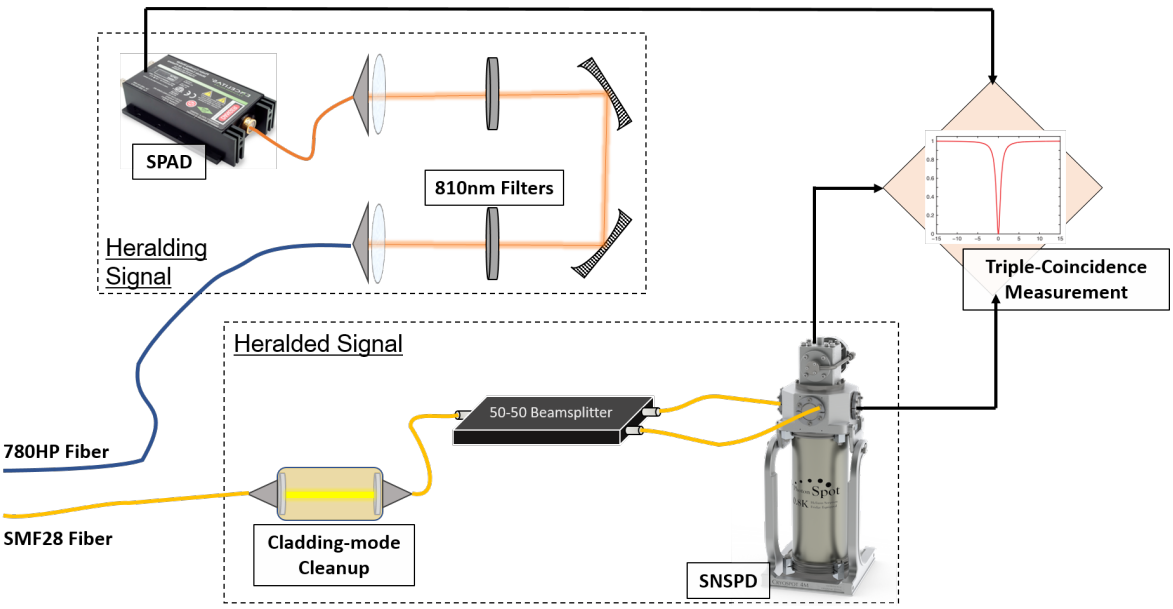

Figure 4.11: Schematic of heralded g(2) setup - The telecom channel is split into two using a 50-50 beam splitter. A triple coincidence measurement is taken with these two outputs and the heralding 810nm photon.

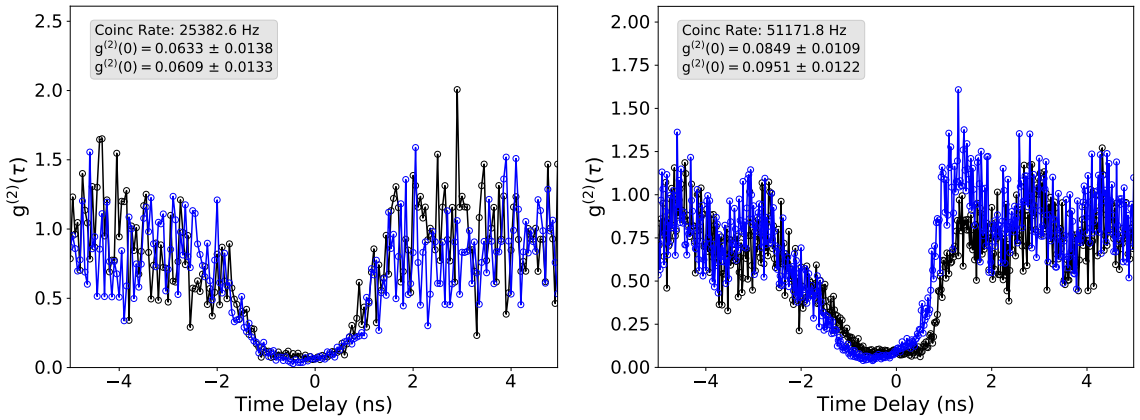

(a) $g^{(2)}(0) < 0.07$ measured with spectral filtering.

(b) $g^{(2)}(0) < 0.09$ measured without spectral filtering.

Figure 4.12: Triple Coincidence Measurements with (a) and without (b) spectral filtering on the telecom photons.

The measurement is taken as shown in fig. 4.11. The visible beam is used as the heralding signal to denote the presence of the telecom herladed signal. The 1550nm photon beam is passed through a 50-50 beam splitter and both the outputs are routed to the SNSPD. Post-detection, we look for coincidences between these two outputs whenever a 810nm photon was also detected. If we had a true-single photon source, detection of the heralding photon would project the heralded signal in a single photon state. In that case, the two outputs beams of the beam splitter should be perfectly anti-correlated giving a $g^{(2)}(0) = 0$. However, it is never the case in reality due to noise in the channel, finite temporal resolution of the detectors and occasional multi-photon pairs in the downconverted field. The experiment was conducted for both the filtered and non-filtered case and the results were found to be much lower than the 0.5 theoretical maximum as shown in fig. 4.12.

Chapter 5

Results and Discussion

5.1 Performance of KTP-QPIC Integrated Platform

1. The integrated WDM structure on the KTP crystal was shown to be extremely efficient at separating the two downconverted photons onto separate waveguides. Over 94% of 1550nm photons were shown to successfully couple to the adjacent waveguide as shown in fig. 5.1(a).

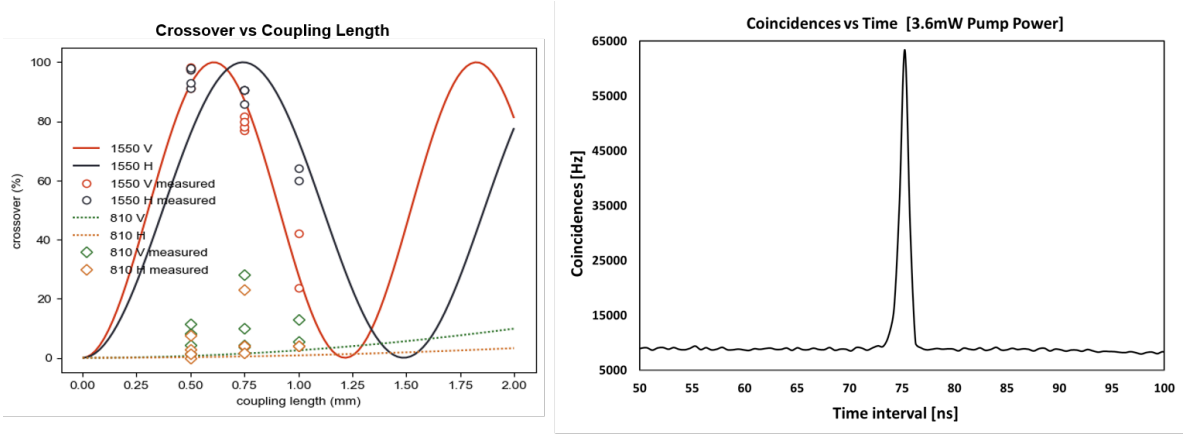

(a) (b)

Figure 5.1: (a) WDM Characterization on the KTP chip. (b) The peak coincidence measured in the KTP-QPIC system was nearly 65k pairs per second at a pump power of 3.6mW.

2. The feasibility of photons coupling from a nonlinear crystal to a photonic waveguide while retaining the quantum correlations has been successfully demonstrated. This is evidenced by the high coincidence peaks witnessed between the KTP and QPIC waveguide outputs as shown in fig. 5.1(b).

3. The pair detection rates with different configurations are shown in table 5.1. The coupling efficiency of the KTP-QPIC interface can now be quantified using the data obtained from the individual characterization experiments. The detected count rate can is defined as follows -

$$\text{Detected Counts} = \text{Generated Counts} \times \text{Losses} \times \text{Detector Efficiency}$$

Considering the path of the telecom photon, in the case of no spectral filters, all losses come from the coupling at the KTP-QPIC interface, QPIC-SMF28 interface and the propagation losses on the QPIC waveguide itself. From section 4.1, we know that -

$$\text{Propagation Loss for a 2mm Si Waveguide at 1550nm} = 0.74 \text{ dB/cm} \times 0.2 \text{ cm}$$

$$\text{QPIC-SMF28 insertion loss} = 1.5 \text{ dB}.$$

Configuration	**Pair detection rate (kHz/mW)**
PPKTP only (with filter)	61.982
PPKTP-QPIC (with filter)	91.048
PPKTP-QPIC (without filter)	128.941

Table 5.1: Pair Detection Rates of different setups.

This gives a net loss of 1.648dB which translates to 68.42% transmission. We can

now determine the KTP-QPIC coupling efficiency as -

$$\frac{\text{Detected rate}}{\text{Generated Rate} \times \text{QPIC Transmission} \times \text{Detected Efficiency}}$$

Previous studies on PPKTP waveguides of similar dimensions [79] have estimated the pair generation rate to be within the range of $5 - 15$ MHz/mW. Using these values, it can be seen that -

$$\begin{aligned}\text{KTP-QPIC Coupling} &= \frac{2.2 \times 10^6}{(5 - 15 \times 10^6)(0.6842)(0.80)} \\ &= 81.11 - 26.79\%.\end{aligned}$$

It is seen that depending on the pair generation rate in the KTP waveguides, anywhere from 26% to 80% photons successfully couple to the QPIC waveguides and are detected. Thus, the feasibility of integrating QPICs with poled nonlinear waveguides is demonstrated as a scalable source of correlated photons.

4. It was also shown that Silicon waveguides on the QPIC could be successfully used to replace bandpass filters on the telecom channel for removing pump noise. While the peak CAR value dropped without filters, it is still higher compared to previous approaches as shown in fig. 5.2.

5. $g^{(2)}(0)$ values of 0.07 and 0.09 were measured for the filtered and non-filtered cases respectively, even at high pump powers. This denotes that the system is very much in the single-photon regime even without bandpass filters.

6. We have also measured extremely low insertion losses (less than 1dB) in other QPIC edge coupler designs which could further enhance the efficiency of this system.

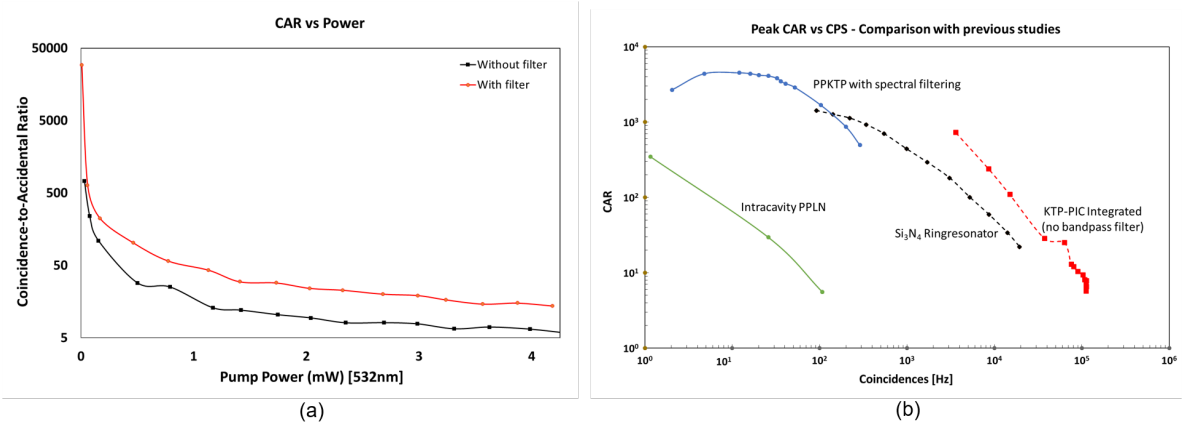

Figure 5.2: Filterless operation - (a) Comparison of CAR with and without bandpass filters on the telecom channel. (b) Comparison of peak CAR vs Coincidence rate with previous studies using PPLN [50], PPKTP [48] and an on-chip SiN ringresonator source [65]. It can be seen that even without bandpass filters, our system has better Peak CAR values for comparable pair rates than previous experiments.

5.2 Next Steps

Now that the feasibility of coupling QPICs to PPKTP is verified, the next steps would be to design QPICs dedicated for quantum operations such as quantum encoding and entanglement. Meanwhile, it is also important to identify a reliable method to package the KTP-PIC system as a single monolithic unit. Experiments to determine how long the heralded telecom photon can travel in an optic fiber without losing the encoded quantum state should follow. The ultimate goal is to use these dedicated systems to demonstrate long-distance quantum entanglement between different quantum nodes.

The success of the integrated WDM also opens up opportunities to design more sophisticated circuits on the KTP itself. These can be be used in very interesting quantum optics experiments like the two-color Hong-Ou-Mandel interference effect.

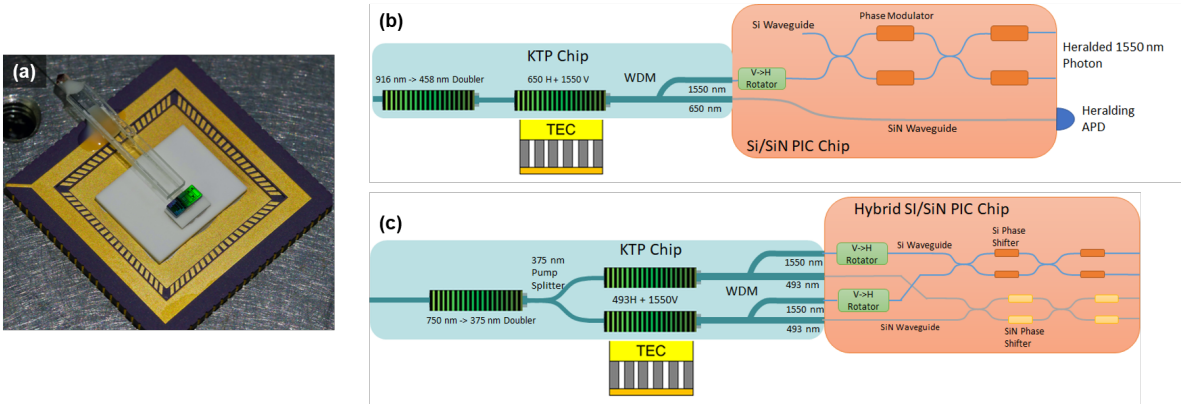

Figure 5.3: Next Steps - (a) Model of a packaged KTP-QPIC unit. (b) Sample schematic of a dual band QPIC capable of heralded photon detection. (c) Sample schematic of a dual band QPIC used to convert polarization entanglement to path entanglement using two different poled regions on a single KTP chip.

5.2.1 On-chip Polarization Handling

Due to the birefringence of Silicon and Silicon Nitride, most photonics components are very sensitive to polarization. As a first step towards designing the dedicated QPICs, it is necessary to have a device that converts the vertical photons generated in the KTP to horizontal polarization. This would greatly simplify the design process of the QPICs because otherwise we would have to design two sets of every circuit, each optimized for one polarization.

Polarization Rotators (PR) use phase-matching [80] or mode-evolution [81] to convert between the transverse-electric (TE) and transverse-magnetic (TM) modes. In either case, the orthogonality of the TE and TM modes must be broken and this is done by breaking the symmetry of the effective index profile both horizontally and vertically. Horizontal symmetry is broken by varying the geometry of the waveguides gradually using tapers. Adding etched layers or having an air cladding on top breaks the vertical symmetry.

Directional Couplers (DC) with lateral tapered sections with widths chosen for phase

matching between TE and TM modes have been shown to rotate polarizations by direct TM0->TE0 rotation or by evolution to a higher order mode : TM0->TE1, followed by rotation to the fundamental mode : TE1->TE0. The coupler lengths can be shortened considerably using a dual-core Si_3N_4-Si waveguide for stronger birefringence [82].

In the case of Mode-evolution-based rotators, the polarization of the light changes as the geometry of the waveguide is gradually varied to mimic physically twisting the waveguide to rotate its axis. Since the cross-section varies in the vertical direction as well, this method is harder to fabricate in the top-down process but the devices have a much smaller footprint compared to the DC-based-rotators. Dual-layered waveguides and waveguides with trenches have been shown to produce ultra compact rotators. This can also be enhanced by tapering each layer and by using layers of different materials [83]. A bi-level tapered section can also be used to rotate and act as a 50-50 splitter similar to a microwave magic-T with adiabatic performance [84]. Combinations of these methods have been employed to further shorten device footprints and minimize crosstalk using multimode waveguides and cascading adiabatic and bent couplers. Rapid adiabatic couplers designed using parameterized functions to suppress unwanted mode conversions have also been used in combination with the Magic-T and tapered waveguides to realize ultra-compact footprints (100mx2m) with record low crosstalk <-14dB. Other alternate methods for polarization rotation using more exotic materials include twisted waveguides made of SU-8 polymer on silica substrate which were shown to be capable of rotating light in both the telecom band and visible spectrum [85] and a dielectric metasurface structure made of subwavelength periodic perturbations for mode conversion. However, these methods are yet to be fully compatible with SOI foundry processes.

We chose to employ a Magic-T section for rotating TM0 light to TE1 and a following phase-matched DC section to convert the TE1 mode to TE0. The Magic-T section

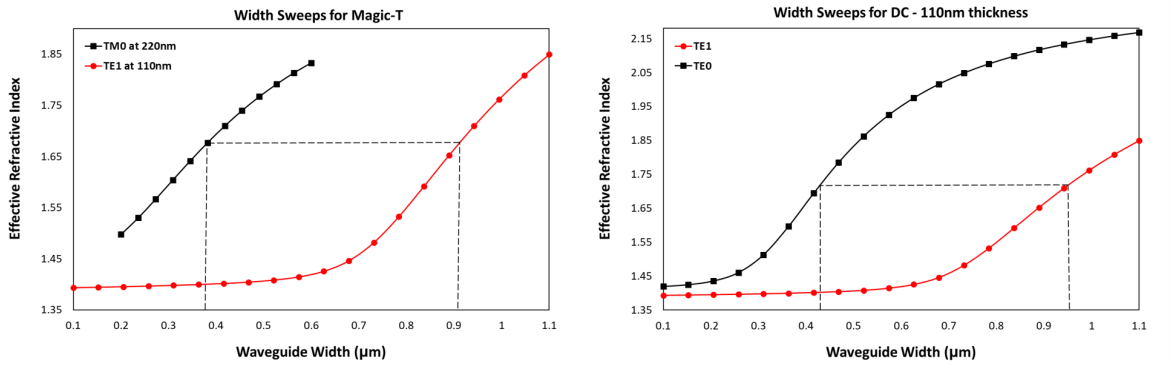

Figure 5.4: (a) It's seen that the effective index of TM0 for a 370nm wide waveguide at 220nm thickness was close to the effective index of TE1 for a 900nm waveguide at 110nm thickness. Hende, for any widths greater than 900nm, the TE1 mode will dominate. Therefore the input and output widths of the Magic-T section were chosen to be 370nm and 970nm respectively. (b) The output of the Magic-T becomes the wide input waveguide of the DC section at 970x110nm. The TE1 mode at this width is phase-matched to the TE0 mode at 445nm, which is chosen as the width of the narrow output waveguide.

consists of two oppositely tapered regions laid on top of each other. This has inherent vertical asymmetry allowing us to have a glass cladding on top of the chip. The DC section consists of a wide and narrow waveguide separated by a small gap allowing for one mode to couple to the other while undergoing mode conversion. Using two different methods for each step allows for a much smaller device footprint than relying on just one. Preliminary simulations were conducted on Ansys Lumerical 2D Eigenmode Evolution (EME) solvers. We were restricted to only two thicknesses of Silicon by the AIM foundry processes - 110nm and 220nm. Different waveguide widths were simulated at either thickness to identify mode crossings. The device dimensions were then optimized using fully 3D Finite-Domain-Time-Difference (FDTD) solvers.

For the magic-T section, the input section is 220nm thick while the output is 110nm thick. The widths were chosen such that the effective index of the TE1 mode at the output is greater than that of the TM0 mode at the input. The length is then optimized

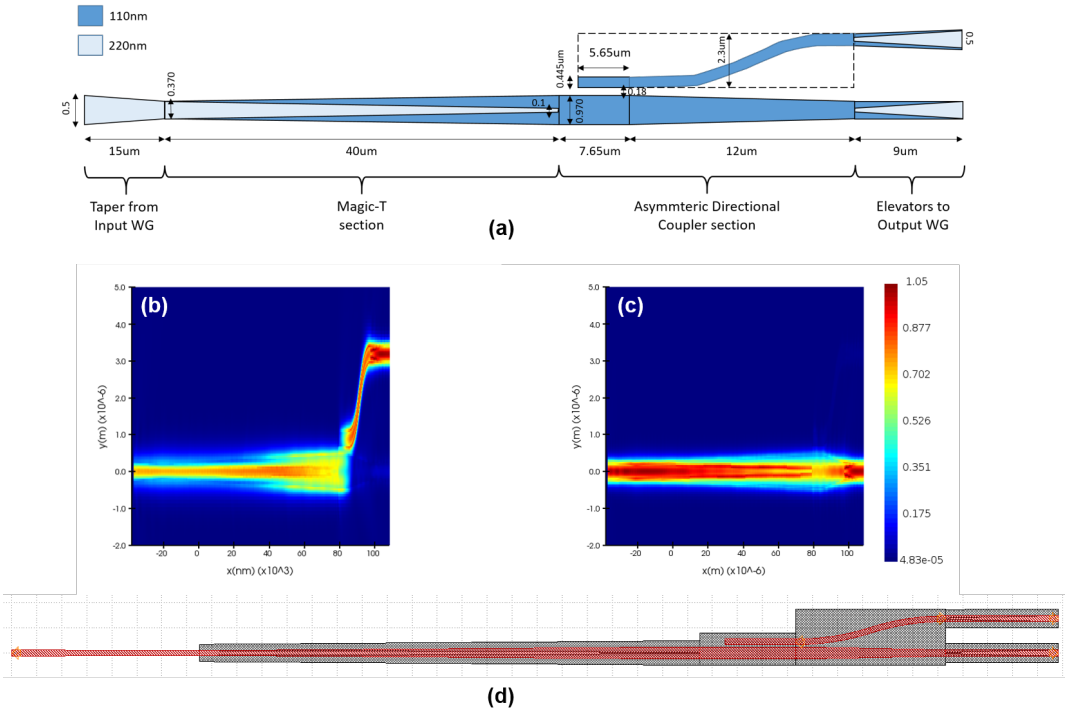

Figure 5.5: Compact Polarization Rotator Design - (a) A sketch of the different sections of the PR. (b) FDTD simulation of TM0->TE1->TE0 conversion. (c) FDTD simulation of TE0->TE0 transmission. (d) Final cell layout of the component that can be directly used in future chip designs viewed in KLayout fully compatible with AIM foundry's fab process.

for maximum mode conversion. For the Asymmetric DC section, both the waveguides are 110nm thick. In this case, the waveguide widths are chosen such that the effective indices of the TE1 mode in the wide waveguide is equal to that of the TE0 mode in the narrow waveguide. The gap between the waveguides is then optimized for using further simulations. The width sweeps used to determine these dimensions are shown in fig.5.4.

Other components such as an S-bend to separate the two outputs, and elevator/taper sections to connect this device to the standard 500x220nm Silicon waveguide were designed separately and optimized. Finally the entire device was modelled in Lumerical FDTD to obtain the various S-parameters to test device efficiency. It was observed that, at a total device length of 83.65μm, 94% of input TM0 mode was successfully converted

to the TE0 mode. This is much more compact than the current available polarization rotator (400μm) with AIM Foundry's design kit. A layout of the device was then created using Nazca Design to be used in future chip designs as shown in fig. 5.5.

5.3 Summary

In this thesis, we have demonstrated a plug-and-play, highly non-degenerate photon pair source efficiently coupled to a QPIC. The system produces higher pair rates than state-of-art on-chip Si_3N_4 resonant sources. High CAR values have been shown utilizing Si waveguides as pump light filters for the first time, thus greatly reducing losses due to spectral filters in previous nonlinear crystal sources. Design of a polarization rotator for future KTP integrated QPICs was also computationally investigated.
This work will enable the bridging of visible wavelength quantum resources and telecom wavelength fiber-optic communication network for reliable long-distance quantum communication in the future.

Acknowledgements

This work was supported by Air Force Research Laboratory (FA8750-20-P-1709). Any opinions, findings, and conclusions or recommendations expressed in this material are those of the author(s) and do not necessarily reflect the views of AFRL.

Permissions obtained for fair use of Images

1. Figure 1.2 - Reprinted with permission from Macmillan Publishers Limited : Springer, Nature, Kimble, H. The quantum internet. Nature 453, 1023–1030 (2008). `https://doi.org/10.1038/nature07127`, © (2008).

2. Figure 2.5 - Open Access under a Creative Commons Attribution 4.0 International License, which permits use, sharing, adaptation, distribution and reproduction in any medium or format. No changes were made to the original image.

3. Figure 2.6 - Open Access under the terms of OSA Open Access Publishing Agreement. No changes were made to the original image.

4. Figure 2.7 - Open Access under the terms of OSA Open Access Publishing Agreement. No changes were made to the original image.

Bibliography

[1] Shohini Ghose. *A Beginner's Guide to Quantum Computing*. Transcript from her talk at Session 3 of TEDWomen 2018. Nov. 29, 2018. URL: `https://www.ted.com/talks/shohini_ghose_a_beginner_s_guide_to_quantum_computing/transcript`.

[2] Richard P Feynman. "Simulating physics with computers". In: *Feynman and computation*. CRC Press, 2018, pp. 133–153.

[3] David Deutsch. "Quantum theory, the Church–Turing principle and the universal quantum computer". In: *Proceedings of the Royal Society of London. A. Mathematical and Physical Sciences* 400.1818 (1985), pp. 97–117.

[4] Peter W Shor. "Algorithms for quantum computation: discrete logarithms and factoring". In: *Proceedings 35th annual symposium on foundations of computer science*. Ieee. 1994, pp. 124–134.

[5] Lov K Grover. "A fast quantum mechanical algorithm for database search". In: *Proceedings of the twenty-eighth annual ACM symposium on Theory of computing*. 1996, pp. 212–219.

[6] Charles H Bennett and Stephen J Wiesner. "Communication via one-and two-particle operators on Einstein-Podolsky-Rosen states". In: *Physical review letters* 69.20 (1992), p. 2881.

[7] John Preskill. "Quantum Computing in the NISQ era and beyond". In: *Quantum* 2 (2018), p. 79.

[8] *IBM's Roadmap For Scaling Quantum Technology*. Nov. 2020. URL: https://www.ibm.com/blogs/research/2020/09/ibm-quantum-roadmap/.

[9] JM Arrazola et al. "Quantum circuits with many photons on a programmable nanophotonic chip". In: *Nature* 591.7848 (2021), pp. 54–60.

[10] Khabat Heshami et al. "Quantum memories: emerging applications and recent advances". In: *Journal of modern optics* 63.20 (2016), pp. 2005–2028.

[11] Marcello Caleffi, Angela Sara Cacciapuoti, and Giuseppe Bianchi. "Quantum Internet: From communication to distributed computing!" In: *Proceedings of the 5th ACM International Conference on Nanoscale Computing and Communication*. 2018, pp. 1–4.

[12] Anil Ananthaswamy. *The Quantum Internet Is Emerging, One Experiment at a Time*. 2019. URL: https://www.scientificamerican.com/article/the-quantum-internet-is-emerging-one-experiment-at-a-time/ (visited on 06/19/2019).

[13] Artur K Ekert. "Quantum cryptography based on Bell's theorem". In: *Physical review letters* 67.6 (1991), p. 661.

[14] Charles H Bennett et al. "Experimental quantum cryptography". In: *Journal of cryptology* 5.1 (1992), pp. 3–28.

[15] Iulia M Georgescu, Sahel Ashhab, and Franco Nori. "Quantum simulation". In: *Reviews of Modern Physics* 86.1 (2014), p. 153.

[16] Stefano Pirandola et al. "Advances in photonic quantum sensing". In: *Nature Photonics* 12.12 (2018), pp. 724–733.

[17] Zheshen Zhang and Quntao Zhuang. "Distributed quantum sensing". In: *Quantum Science and Technology* (2020).

[18] Mario Krenn et al. "Quantum communication with photons". In: *Optics in Our Time* 18 (2016), p. 455.

[19] H Jeff Kimble. "The quantum internet". In: *Nature* 453.7198 (2008), pp. 1023–1030.

[20] Kyung Soo Choi et al. "Mapping photonic entanglement into and out of a quantum memory". In: *Nature* 452.7183 (2008), pp. 67–71.

[21] Fulvio Flamini, Nicolo Spagnolo, and Fabio Sciarrino. "Photonic quantum information processing: a review". In: *Reports on Progress in Physics* 82.1 (2018), p. 016001.

[22] S Olmschenk et al. "Quantum teleportation between distant matter qubits". In: *Science* 323.5913 (2009), pp. 486–489.

[23] L-M Duan and Christopher Monroe. "Colloquium: Quantum networks with trapped ions". In: *Reviews of Modern Physics* 82.2 (2010), p. 1209.

[24] Stephan Ritter et al. "An elementary quantum network of single atoms in optical cavities". In: *Nature* 484.7393 (2012), pp. 195–200.

[25] Bas Hensen et al. "Loophole-free Bell inequality violation using electron spins separated by 1.3 kilometres". In: *Nature* 526.7575 (2015), pp. 682–686.

[26] Nicolas Maring et al. "Photonic quantum state transfer between a cold atomic gas and a crystal". In: *Nature* 551.7681 (2017), pp. 485–488.

[27] Colin D Bruzewicz et al. "Trapped-ion quantum computing: Progress and challenges". In: *Applied Physics Reviews* 6.2 (2019), p. 021314.

[28] David S Weiss and Mark Saffman. "Quantum computing with neutral atoms". In: *Physics Today* 70.7 (2017).

[29] JR Weber et al. "Quantum computing with defects". In: *Proceedings of the National Academy of Sciences* 107.19 (2010), pp. 8513–8518.

[30] A Imamog et al. "Quantum information processing using quantum dot spins and cavity QED". In: *Physical review letters* 83.20 (1999), p. 4204.

[31] Sylvain Bertaina et al. "Rare-earth solid-state qubits". In: *Nature nanotechnology* 2.1 (2007), pp. 39–42.

[32] William K Wootters and Wojciech H Zurek. "A single quantum cannot be cloned". In: *Nature* 299.5886 (1982), pp. 802–803.

[33] Dik Bouwmeester et al. "Experimental quantum teleportation". In: *Nature* 390.6660 (1997), pp. 575–579.

[34] MD Eisaman et al. "Single-photon sources and detectors (Invited Review Article)". In: *Rev. Sci. Instrum* 82 (2011), pp. 071101–25.

[35] SA Castelletto and RE Scholten. "Heralded single photon sources: a route towards quantum communication technology and photon standards". In: *The European Physical Journal Applied Physics* 41.3 (2008), pp. 181–194.

[36] Robert W Boyd. *Nonlinear optics*. Academic press, 2020.

[37] CK Hong and L Mandel. "Theory of parametric frequency down conversion of light". In: *Physical Review A* 31.4 (1985), p. 2409.

[38] Christophe Couteau. "Spontaneous parametric down-conversion". In: *Contemporary Physics* 59.3 (2018), pp. 291–304.

[39] Keiichi Edamatsu. "Entangled photons: generation, observation, and characterization". In: *Japanese Journal of Applied Physics* 46.11R (2007), p. 7175.

[40] David S Hum and Martin M Fejer. "Quasi-phasematching". In: *Comptes Rendus Physique* 8.2 (2007), pp. 180–198.

[41] Boris Albrecht et al. "A waveguide frequency converter connecting rubidium-based quantum memories to the telecom C-band". In: *Nature communications* 5.1 (2014), pp. 1–6.

[42] Anaís Dréau et al. "Quantum frequency conversion of single photons from a nitrogen-vacancy center in diamond to telecommunication wavelengths". In: *Physical Review Applied* 9.6 (2018), p. 064031.

[43] Thomas Walker et al. "Long-distance single photon transmission from a trapped ion via quantum frequency conversion". In: *Physical review letters* 120.20 (2018), p. 203601.

[44] Matthias Bock et al. "High-fidelity entanglement between a trapped ion and a telecom photon via quantum frequency conversion". In: *Nature communications* 9.1 (2018), pp. 1–7.

[45] V Krutyanskiy et al. "Light-matter entanglement over 50 km of optical fibre". In: *npj Quantum Information* 5.1 (2019), pp. 1–5.

[46] Dirk Richter et al. "Tunable Difference Frequency Generation Laser Spectrometers: Successes, Challenges, and Opportunities". In: *Laser Applications to Chemical, Security and Environmental Analysis*. Optical Society of America. 2010, LMA4.

[47] Sylvain Fasel et al. "High-quality asynchronous heralded single-photon source at telecom wavelength". In: *New Journal of Physics* 6.1 (2004), p. 163.

[48] Christoph Clausen et al. "A source of polarization-entangled photon pairs interfacing quantum memories with telecom photons". In: *New Journal of Physics* 16.9 (2014), p. 093058.

[49] Oliver Slattery et al. "Narrow-linewidth source of greatly non-degenerate photon pairs for quantum repeaters from a short singly resonant cavity". In: *Applied Physics B* 121.4 (2015), pp. 413–419.

[50] Daniel Rieländer et al. "Cavity enhanced telecom heralded single photons for spin-wave solid state quantum memories". In: *New Journal of Physics* 18.12 (2016), p. 123013.

[51] Gerhard Schunk et al. "Interfacing transitions of different alkali atoms and telecom bands using one narrowband photon pair source". In: *Optica* 2.9 (2015), pp. 773–778.

[52] Je-Hyung Kim et al. "Hybrid integration methods for on-chip quantum photonics". In: *Optica* 7.4 (2020), pp. 291–308.

[53] Zhiping Zhou, Bing Yin, and Jurgen Michel. "On-chip light sources for silicon photonics". In: *Light: Science & Applications* 4.11 (2015), e358–e358.

[54] C Schuck, WHP Pernice, and HX Tang. "NbTiN superconducting nanowire detectors for visible and telecom wavelengths single photon counting on Si3N4 photonic circuits". In: *Applied Physics Letters* 102.5 (2013), p. 051101.

[55] Graham T Reed. "Silicon photonics: the state of the art". In: (2008).

[56] Jay E Sharping et al. "Generation of correlated photons in nanoscale silicon waveguides". In: *Optics express* 14.25 (2006), pp. 12388–12393.

[57] Stéphane Clemmen et al. "Continuous wave photon pair generation in silicon-on-insulator waveguides and ring resonators". In: *Optics express* 17.19 (2009), pp. 16558–16570.

[58] Justin B Spring et al. "On-chip low loss heralded source of pure single photons". In: *Optics express* 21.11 (2013), pp. 13522–13532.

[59] Jeffrey A Steidle et al. “High spectral purity silicon ring resonator photon-pair source”. In: *Quantum Information and Computation XIII*. Vol. 9500. International Society for Optics and Photonics. 2015, p. 950015.

[60] Ryota Wakabayashi et al. “Time-bin entangled photon pair generation from Si micro-ring resonator”. In: *Optics express* 23.2 (2015), pp. 1103–1113.

[61] Tin Komljenovic et al. “Heterogeneous silicon photonic integrated circuits”. In: *Journal of Lightwave Technology* 34.1 (2016), pp. 20–35.

[62] Xiaoxi Wang et al. “Photon pair generation using silicon photonic microring and hybrid laser”. In: *CLEO: Applications and Technology*. Optical Society of America. 2017, JTh5C–6.

[63] Chaoxuan Ma et al. “Silicon photonic entangled photon-pair and heralded single photon generation with CAR$>$ 12,000 and g (2)(0)$<$ 0.006”. In: *Optics Express* 25.26 (2017), pp. 32995–33006.

[64] CC Tison et al. “Path to increasing the coincidence efficiency of integrated resonant photon sources”. In: *Optics Express* 25.26 (2017), pp. 33088–33096.

[65] Xiyuan Lu et al. “On-chip optical parametric oscillation into the visible: generating red, orange, yellow, and green from a near-infrared pump”. In: *Optica* 7.10 (2020), pp. 1417–1425.

[66] Xiyuan Lu et al. “Chip-integrated visible–telecom entangled photon pair source for quantum communication”. In: *Nature physics* 15.4 (2019), pp. 373–381.

[67] Lucia Caspani et al. “Integrated sources of photon quantum states based on nonlinear optics”. In: *Light: Science & Applications* 6.11 (2017), e17100–e17100.

[68] Alexander W Bruch et al. “On-chip χ (2) microring optical parametric oscillator”. In: *Optica* 6.10 (2019), pp. 1361–1366.

[69] Jie Zhao et al. “High quality entangled photon pair generation in periodically poled thin-film lithium niobate waveguides”. In: *Physical review letters* 124.16 (2020), p. 163603.

[70] Osama Terra, Hatem Hussein, and Johan Burger. “Investigation of bulk and waveguide frequency doubling crystals for interrogation of a two-photon transition in rubidium”. In: *Optik-International Journal for Light and Electron Optics* 126.19 (2015), pp. 1792–1796.

[71] Toshiaki Suhara. “Generation of quantum-entangled twin photons by waveguide nonlinear-optic devices”. In: *Laser & Photonics Reviews* 3.4 (2009), pp. 370–393.

[72] V Ya Shur et al. “Periodically poled crystals of KTP family: a review”. In: *Ferroelectrics* 496.1 (2016), pp. 49–69.

[73] Laura Padberg et al. “Characterisation of width-dependent diffusion dynamics in rubidium-exchanged KTP waveguides”. In: *Optics Express* 28.17 (2020), pp. 24353–24362.

[74] Justin E Christensen et al. “High-fidelity manipulation of a qubit enabled by a manufactured nucleus”. In: *npj Quantum Information* 6.1 (2020), pp. 1–5.

[75] John D Bierlein et al. “Fabrication and characterization of optical waveguides in KTiOPO4”. In: *Applied Physics Letters* 50.18 (1987), pp. 1216–1218.

[76] Lukas Chrostowski and Michael Hochberg. “Silicon photonics design: from devices to systems”. In: Cambridge University Press, 2015. Chap. 04.

[77] Yachen Gao et al. “Saturable absorption and reverse saturable absorption in platinum nanoparticles”. In: *Optics communications* 251.4-6 (2005), pp. 429–433.

[78] E Bocquillon et al. “Coherence measures for heralded single-photon sources”. In: *Physical Review A* 79.3 (2009), p. 035801.

[79] Marco Fiorentino et al. “Spontaneous parametric down-conversion in periodically poled KTP waveguides and bulk crystals”. In: *Optics express* 15.12 (2007), pp. 7479–7488.

[80] Daoxin Dai, Yongbo Tang, and John E Bowers. “Mode conversion in tapered submicron silicon ridge optical waveguides”. In: *Optics express* 20.12 (2012), pp. 13425–13439.

[81] MR Watts and HA Haus. “Integrated mode-evolution-based polarization rotators”. In: *Optics letters* 30.2 (2005), pp. 138–140.

[82] Weimin Ye et al. “Design of broadband silicon-waveguide mode-order converter and polarization rotator with small footprints”. In: *Optics Express* 25.26 (2017), pp. 33176–33183.

[83] Wesley D Sacher et al. “Polarization rotator-splitters in standard active silicon photonics platforms”. In: *Optics express* 22.4 (2014), pp. 3777–3786.

[84] Milos A Popovic and Anatol Khilo. “Integrated photonic magic-T (with twice the magic)”. In: *Integrated Photonics Research, Silicon and Nanophotonics*. Optical Society of America. 2010, IWG7.

[85] Zhi-Shan Hou et al. “On-Chip Polarization Rotators”. In: *Advanced Optical Materials* 7.10 (2019), p. 1900129.